

On Retrospective k -space Subsampling schemes For Deep MRI Reconstruction

George Yiasemis^a, Clara I. Sánchez^b, Jan-Jakob Sonke^a, Jonas Teuwen^{a,b,c}

^aAI for Oncology, Netherlands Cancer Institute, Plesmanlaan 121, Amsterdam, 1066 CX, Netherlands

^bUniversity of Amsterdam, Science Park 904, Amsterdam, 1098 XH, Netherlands

^cRadboud University Medical Center, Department of Medical Imaging, Geert Grooteplein Zuid 10, Nijmegen, 6525 GA, Netherlands

Abstract

Acquiring fully-sampled MRI k -space data is time-consuming, and collecting accelerated data can reduce the acquisition time. Employing 2D Cartesian-rectilinear subsampling schemes is a conventional approach for accelerated acquisitions; however, this often results in imprecise reconstructions, even with the use of Deep Learning (DL), especially at high acceleration factors. Non-rectilinear or non-Cartesian trajectories can be implemented in MRI scanners as alternative subsampling options. This work investigates the impact of the k -space subsampling scheme on the quality of reconstructed accelerated MRI measurements produced by trained DL models. The Recurrent Variational Network (RecurrentVarNet) was used as the DL-based MRI-reconstruction architecture. Cartesian, fully-sampled multi-coil k -space measurements from three datasets were retrospectively subsampled with different accelerations using eight distinct subsampling schemes: four Cartesian-rectilinear, two Cartesian non-rectilinear, and two non-Cartesian. Experiments were conducted in two frameworks: scheme-specific, where a distinct model was trained and evaluated for each dataset-subsampling scheme pair, and multi-scheme, where for each dataset a single model was trained on data randomly subsampled by any of the eight schemes and evaluated on data subsampled by all schemes. In both frameworks, RecurrentVarNets trained and evaluated on non-rectilinearly subsampled data demonstrated superior performance, particularly for high accelerations. In the multi-scheme setting, reconstruction performance on rectilinearly subsampled data improved when compared to the scheme-specific experiments. Our findings demonstrate the potential for using DL-based methods, trained on non-rectilinearly subsampled measurements, to optimize scan time and image quality.

Keywords: Deep MRI Reconstruction, Retrospective k -space Subsampling, Non-rectilinear Subsampling, Non-Cartesian Subsampling, Recurrent Variational Network

1. Introduction

Magnetic Resonance Imaging (MRI) is a widely used medical imaging modality known for its ability to produce high soft tissue contrast, high-resolution images without the use of ionizing radiation. Its applications range from diagnosis and treatment planning to real-time MR-guided tasks such as surgery or radiotherapy. However, the long acquisition times of the MRI measurements, known as k -space, hinder the full potential of MRI-guidance. Reducing these times could make MRI-guidance cheaper and extend its functionality in real-time settings.

Over the past two decades, several methods have been put to use in clinical practice for accelerating the MRI acquisition. The two most conventionally applied methods to-date are Parallel Imaging (PI) and Compressed Sensing (CS), which are usually both incorporated in modern state-of-the-art MRI scanners.

Compressed Sensing aims to reconstruct images from incoherently subsampled k -space measurements through mathematical optimization techniques [1, 2, 3, 4]. Subsampling the k -space is, in general, a violation of the Nyquist-Shannon sampling criterion [5] and thus prone to producing aliasing artifacts. CS reconstruction algorithms employ optimization methods like Total Variation (TV) [6] to obtain faithful images from sparse input signals.

Parallel Imaging on the other hand, employs an array of multiple - instead of one - radio-frequency receiver coils which measure sets of spatially localised k -space frequencies while maintaining the same spatial resolution [7, 8, 9]. Each independent receiver coil receives distinct measurements corresponding to their spatial location in relation to the scanned object.

With the recent advancements in Deep Learning (DL) and Computer Vision (CV), a plethora of algorithms have emerged targeting to solve imaging inverse problems, with Accelerated MRI Reconstruction being a par excellence example. By utilizing CS optimization approaches and PI, numerous DL-based methods involving convolutional neural networks (CNNs) have been proposed in the literature [10, 11, 12, 13, 14, 15] applied to the task of Accelerated MRI Reconstruction. These methods are usually trained in a supervised manner using retrospectively subsampled (from available fully-sampled) k -space datasets and their target is to make a prediction of the fully-sampled k -space or its image reconstruction.

Rectilinear Cartesian patterns constitute the most commonly applied subsampling techniques in clinical 2D MRI acquisitions. Subsequently, DL-based Accelerated MRI Reconstruction applications utilize rectilinear subsampling masks to retrospectively subsample fully-sampled data. However, a variety of prospective and retrospective non-rectilinear Cartesian

sampling and subsampling patterns exist. For instance, non-Cartesian patterns such as radial or spiral are being applied in real-time MRI acquisitions due to the fact that they are less susceptible to motion compared to Cartesian ones [16]. The authors in [17] by employing a deep neural network architecture, namely the Recurrent Inference Machine (RIM) [12], explored the effects of training RIMs by applying either rectilinear or radial retrospective subsampling, and concluded that the RIM trained using the latter could produce higher-fidelity reconstructions.

In this work, we aim to investigate and compare the effects of employing various retrospective subsampling schemes on the quality of DL-based learned image reconstructions. To that end, we trained and tested Recurrent Variational Networks [15] (RecurrentVarNets) on retrospectively subsampled k -space measurements. We performed experiments under either scheme-specific or multi-scheme setups, in which models were trained and evaluated on data subsampled with either individual or multiple, respectively, subsampling schemes.

The contributions and findings of our work can be summarized as follows:

- We provide a review of eight currently employed (retrospective) subsampling techniques.
- We experimentally show that DL models trained and evaluated on non-rectilinearly, compared to rectilinearly, subsampled data output superior reconstructions, especially for high acceleration factors.
- We demonstrate that models trained on data subsampled with multiple instead of individual patterns, can reconstruct rectilinearly subsampled data with higher fidelity.

2. Background - Theory

2.1. MRI Acquisition

MRI reconstruction is an inverse problem on account of the fact that MR scanners acquire MRI measurements in the spatial-frequency domain, also known as the Fourier space, and an inversion procedure is required to produce the desired MR image.

Let $n = n_x \times n_y$ denote the spatial size of the reconstructed data. In the case of single-coil acquisition, the relationship between the underlying (vectorized) image $\mathbf{x} \in \mathbb{C}^n$ and the (vectorized) single-channel k -space $\mathbf{y} \in \mathbb{C}^n$ is given by

$$\mathbf{y} = \mathcal{F}(\mathbf{x}) + \mathbf{e}, \quad (1)$$

where \mathcal{F} denotes the two-dimensional (Fast) Fourier Transform (FFT) and $\mathbf{e} \in \mathbb{C}^n$ some measurement noise.

2.1.1. Parallel MRI Acquisition

In PI, multiple receiver coils are placed around the subject to speed up the acquisition. Assuming a number of n_c coils, the acquired (multi-channel) k -space measurements are given by

$$\mathbf{y} = (\mathbf{y}^1, \dots, \mathbf{y}^{n_c}) \in \mathbb{C}^{n \times n_c}, \quad (2)$$

$$\mathbf{y}^k = \mathcal{F}(\mathbf{S}^k \mathbf{x}) + \mathbf{e}^k, \quad k = 1, 2, \dots, n_c,$$

where \mathbf{e}^k denotes noise measured by the k^{th} coil and $\mathbf{S}^k \in \mathbb{C}^{n \times n}$ the sensitivity map of the k^{th} coil expressed as a diagonal complex matrix. Within each coil's reception region, these maps encode their spatial sensitivity by measuring the relative weighting of signals acquired from various locations within the subject. The sensitivity maps are usually normalized as follows

$$\sum_{k=1}^{n_c} \mathbf{S}^{k*} \mathbf{S}^k = \mathbf{I}_n, \quad (3)$$

where \mathbf{S}^{k*} indicates the complex conjugate of \mathbf{S}^k and $\mathbf{I}_n \in \mathbb{R}^{n \times n}$ denotes the n -rank identity matrix.

Obtaining an image from multi-channel measurements \mathbf{y} can be done by using the root-sum-of-squares (RSS) which operates as follows:

$$\mathbf{x}_{\text{RSS}} = \text{RSS}(\hat{\mathbf{x}}^1, \dots, \hat{\mathbf{x}}^{n_c}) = \left(\sum_{k=1}^{n_c} |\hat{\mathbf{x}}^k|^2 \right)^{\frac{1}{2}}, \quad (4)$$

$$\hat{\mathbf{x}}^k = \mathcal{F}^{-1}(\mathbf{y}^k), \quad k = 1, 2, \dots, n_c.$$

2.2. Accelerated MRI Acquisition

To accelerate the MRI acquisition, the k -space is subsampled by collecting fewer than necessary measurements. The subsampling procedure can be described as the application of a subsampling operator \mathbf{U} on the fully-sampled k -space measurements. The subsampled k -space is given by

$$\tilde{\mathbf{y}}^k = \mathbf{U} \mathbf{y}^k = \mathbf{U} \mathcal{F}(\mathbf{S}^k \mathbf{x}) + \tilde{\mathbf{e}}^k, \quad k = 1, 2, \dots, n_c, \quad (5)$$

where $\tilde{\mathbf{e}}^k = \mathbf{U} \mathbf{e}^k$ and \mathbf{U} is expressed as a binary diagonal mask indicating which measurements are sampled as follows:

$$\mathbf{z}_{\mathbf{U}} := (\mathbf{U} \mathbf{z})_i = \begin{cases} \mathbf{z}_i, & \mathbf{U}_{ii} = 1 \\ 0, & \mathbf{U}_{ii} = 0. \end{cases} \quad (6)$$

The magnitude of the acceleration is determined by an acceleration factor R . For a specific R , \mathbf{U} can be chosen such that

$$n \cdot \left(\sum_{i=1}^n \mathbf{U}_{ii} \right)^{-1} \approx R. \quad (7)$$

2.3. Accelerated MRI Reconstruction

2.3.1. Sensitivity Map Estimation

The sensitivity maps $\mathbf{S} = (\mathbf{S}^1, \dots, \mathbf{S}^{n_c})$ can be estimated by various methods found in the literature [18, 7, 19, 20]. A common method for estimating them is by fully-sampling a small region of the center of the k -space, also known as the autocalibration signal (ACS) which includes low frequencies [15, 21].

Let \mathbf{U}_{ACS} denote the ACS-subsampling operator such that when applied on k -space data it outputs the fully-sampled ACS region, i.e.:

$$\mathbf{z}_{\text{acs}} := (\mathbf{U}_{\text{ACS}} \mathbf{z})_i = \begin{cases} \mathbf{z}_i, & i \in \text{ACS region} \\ 0, & \text{otherwise.} \end{cases} \quad (8)$$

Subsequently, to obtain an initial approximation of the sensitivity maps we use the RSS method:

$$\tilde{\mathbf{S}}^k \approx \text{diag}[\mathbf{x}_{\text{acs}}^k \oslash \mathbf{x}_{\text{acs}}], \quad k = 1, 2, \dots, n_c, \quad (9)$$

where \oslash denotes the element-wise division, and

$$\mathbf{x}_{\text{acs}}^k = \mathcal{F}^{-1}(\mathbf{U}_{\text{ACS}} \tilde{\mathbf{y}}^k), \quad \mathbf{x}_{\text{acs}} = \text{RSS}(\{\mathbf{x}_{\text{acs}}^k\}_{k=1}^{n_c}). \quad (10)$$

2.3.2. Accelerated MRI Reconstruction as an Inverse Problem

Obtaining a reconstruction from accelerated multicoil k -space measurements is an inverse problem, with a forward problem given by Eq. 5. We can rewrite Eq. 5 in a more compact notation:

$$\tilde{\mathbf{y}} = \mathcal{A}_{\mathbf{U}, \mathbf{S}}(\mathbf{x}), \quad \mathcal{A}_{\mathbf{U}, \mathbf{S}} := \mathbf{U} \circ \mathcal{F} \circ \mathcal{E}_{\mathbf{S}}, \quad (11)$$

where $\mathcal{A}_{\mathbf{U}, \mathbf{S}} : \mathbb{C}^n \rightarrow \mathbb{C}^{n \times n_c}$ denotes the forward operator and $\mathcal{E}_{\mathbf{S}} : \mathbb{C}^n \rightarrow \mathbb{C}^{n \times n_c}$ is called the expand operator which maps an image $\mathbf{x} \in \mathbb{C}^n$ to the individual coil images using \mathbf{S} :

$$\mathcal{E}_{\mathbf{S}}(\mathbf{x}) = (\mathbf{S}^1 \mathbf{x}, \dots, \mathbf{S}^{n_c} \mathbf{x}). \quad (12)$$

The backward operator of $\mathcal{A}_{\mathbf{U}, \mathbf{S}}$ is given by

$$\mathcal{A}_{\mathbf{U}, \mathbf{S}}^* := \mathcal{R}_{\mathbf{S}} \circ \mathcal{F}^{-1} \circ \mathbf{U} : \mathbb{C}^{n \times n_c} \rightarrow \mathbb{C}^n, \quad (13)$$

where $\mathcal{R}_{\mathbf{S}} : \mathbb{C}^{n \times n_c} \rightarrow \mathbb{C}^n$ is called the reduce operator that combines individual coil images $\mathbf{z} \in \mathbb{C}^{n \times n_c}$ using \mathbf{S} as follows:

$$\mathcal{R}_{\mathbf{S}}(\mathbf{z}) = \sum_{k=1}^{n_c} \mathbf{S}^{k*} \mathbf{z}^k. \quad (14)$$

Note that the operators \mathbf{U} , \mathcal{F} and \mathcal{F}^{-1} in Eq. 11 and Eq. 13 are applied coil-wise.

Subsampling the k -space causes obtaining a solution to Eq. 11 to be an ill-posed inverse problem [22, 23], and therefore, a solution through direct inversion is not feasible. In CS, recovering an estimation of the ground truth image \mathbf{x} from the subsampled MRI measurements $\tilde{\mathbf{y}}$ can be formulated as a solution to a variational optimization problem as follows:

$$\hat{\mathbf{x}} = \underset{\mathbf{w}}{\text{argmin}} \|\mathcal{A}_{\mathbf{U}, \mathbf{S}}(\mathbf{w}) - \tilde{\mathbf{y}}\|_2^2 + \alpha \mathcal{G}(\mathbf{w}), \quad (15)$$

where $\mathcal{G} : \mathbb{C}^n \rightarrow \mathbb{R}$ is a regularization function which can impose prior information about the solution and $\alpha > 0$ is a regularization parameter. In the literature various choices of \mathcal{G} and algorithms for solving Eq. 15 have been employed [24, 25, 26, 27].

2.3.3. Deep Learning-based Accelerated MRI Reconstruction

With the advent of the involvement of DL in MRI reconstruction tasks, the need for handcrafting a specific regularization function has been replaced with CNN-based architectures. A plethora of approaches solve Eq. 15 by unrolling it into a gradient descent iterative optimization scheme over T time-steps:

$$\begin{aligned} \mathbf{w}_{t+1} &= \mathbf{w}_t - \alpha_{t+1} \mathcal{A}_{\mathbf{U}, \mathbf{S}}^*(\mathcal{A}_{\mathbf{U}, \mathbf{S}}(\mathbf{w}_t) - \tilde{\mathbf{y}}) + \mathcal{H}_{\theta_{t+1}}(\mathbf{w}_t), \\ t &= 0, \dots, T-1, \end{aligned} \quad (16)$$

where α_t denotes a (trainable) learning rate and \mathcal{H}_{θ_t} a CNN-based architecture with trainable parameters θ_t . The initial image \mathbf{w}_0 in Eq. 16 can be chosen as a zero-filled reconstruction using $\tilde{\mathbf{y}}$.

Sensitivity maps can be estimated as in Eq. 9 and/or can be refined using another CNN-based model \mathcal{S}_{ψ} with trainable parameters ψ which takes as input the estimation $\tilde{\mathbf{S}} = (\tilde{\mathbf{S}}^1, \dots, \tilde{\mathbf{S}}^{n_c})$ as in Eq. 9:

$$\mathbf{S} = \mathcal{S}_{\psi}(\tilde{\mathbf{S}}). \quad (17)$$

Optimization of Eq. 16 may alternatively be performed in the k -space domain as demonstrated by some authors [21, 15]:

$$\begin{aligned} \mathbf{y}_{t+1} &= \mathbf{y}_t - \alpha_{t+1} \mathbf{U}(\mathbf{y}_t - \tilde{\mathbf{y}}) \\ &\quad + \mathcal{F} \circ \mathcal{E}_{\mathbf{S}} \circ \mathcal{H}_{\theta_{t+1}} \circ \mathcal{R}_{\mathbf{S}} \circ \mathcal{F}^{-1}(\mathbf{y}_t), \end{aligned} \quad (18)$$

with initial condition $\mathbf{y}_0 = \tilde{\mathbf{y}}$.

2.4. k -space Sampling

A sampling scheme or k -space trajectory refers to the course of filling up a complex array with k -space frequencies acquired over a sequence of time-steps during the MRI acquisition. There exist a wide range of 2D k -space trajectories implemented in clinical settings which can be split into two groups: Cartesian and non-Cartesian trajectories.

Cartesian trajectories aim in collecting samples on a Cartesian or equispaced and rectangular grid. The most common Cartesian trajectory is the rectilinear one in which k -space samples are acquired in a line-by-line scheme as illustrated by Figure 1(a) with resulting samples being equidistant in both axes. Note that usually in the literature the Cartesian rectilinear trajectory is referred to as simply *Cartesian*. In this work we use the characterization *Cartesian* to refer to any trajectory acquired on a Cartesian grid.

Non-Cartesian trajectories include schemes such as the radial or the spiral. In the former, k -space signal samples are acquired along several spokes crossing its center (see Figure 1(b)), resulting in the center being sampled multiple times. Meanwhile, the latter includes acquiring data on helical curves starting from the center of the k -space (see Figure 1(c)). In non-Cartesian trajectories, k -space measurements are acquired on a non-Cartesian grid and are therefore not equidistant with each other. For instance, in the radial filling, samples closer to the center are more dense compared to samples further on the radial spokes.

To accelerate the MRI acquisition, the k -space is subsampled by an acceleration factor R , resulting in fewer measurements being collected than those strictly required by the Nyquist-Shannon criterion for perfect reconstruction. This can lead to a degradation of the quality of the reconstruction, depending on the magnitude of the acceleration factor. For instance, for $R = 2$, half of the necessary k -space measurements are acquired. In Figure 1(d)-(f) we provide examples of subsampled k -space trajectories: Cartesian rectilinear (Figure 1(d)), radial and spiral (Figure 1(e)-(f)).

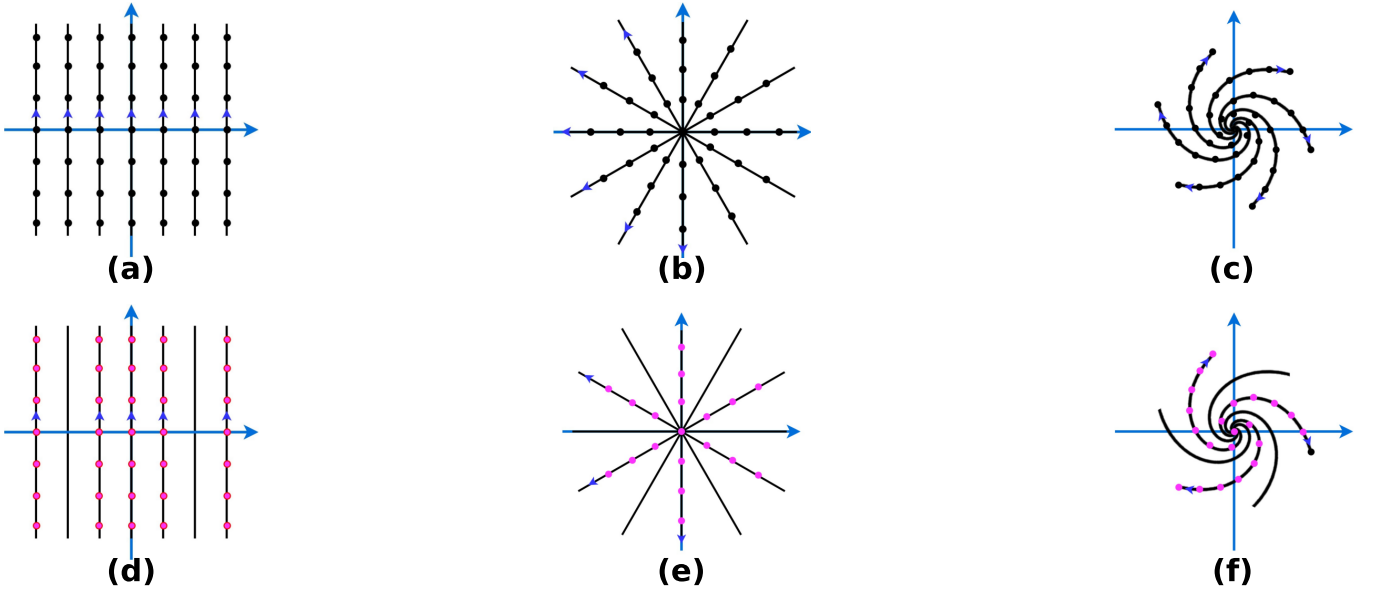


Figure 1: **Top:** k -space sampling trajectories. Cartesian: (a) Rectilinear: k -space is filled in a line-by-line scheme. Non-Cartesian: (b) Radial: k -space is filled with radial spokes passing through the center, (c) Spiral: k -space is filled by one or multiple helical curves. Each line in (a) and (b), and curve in (c), represent a separate filling. The dark blue arrows show the direction of each readout. **Bottom:** Subsampled k -space trajectories for different acceleration factors: (d) Rectilinear, $R \approx 1.5$. (e) Radial, $R \approx 2$. (f) Spiral, $R \approx 2$.

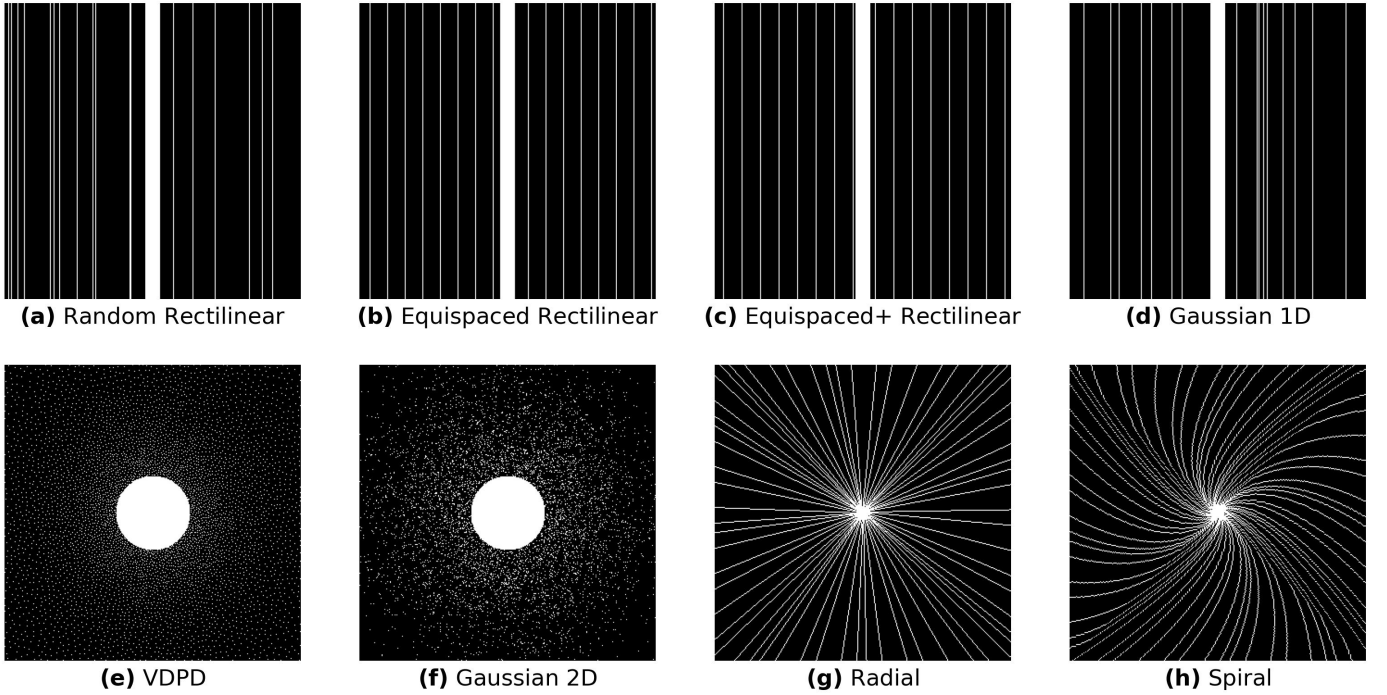


Figure 2: Examples of subsampling masks for Cartesian data for acceleration factor $R = 5$. (a)-(d) Rectilinear: generated by first selecting a fraction of center (ACS) columns. The rest of the columns are: (a) selected uniformly at random, (b) equispaced with a fixed distance, (c) equispaced but symmetric, (d) selected from the Gaussian distribution (e) Variable-density Poisson Disk: generated using Bridson's fast algorithm [28]. (f) Gaussian 2D: samples selected from a 2D Gaussian distribution. For (e)-(f) the ACS region was generated by fully-sampling a centered disk. (g)-(h) Simulated non-Cartesian patterns using the CIRCUS algorithm [29]: (g) Radial, (h) Spiral.

3. Methods

3.1. Retrospective k -space Subsampling

The data used in this work consisted of volumes of fully-sampled raw k -space measurements acquired on a Cartesian

grid. To simulate prospective subsampling we generated 2D subsampling masks which we retrospectively applied onto the fully-sampled multi-coil k -space data to produce subsampled/masked measurements. The generated masks were binary, signifying that a sample from the fully-sampled data was masked if and only if the corresponding mask entry was zero.

As in this work we are interested in studying the role of the subsampling pattern on the quality of DL-based reconstructions of subsampled MRI data, we focused on the following retrospective subsampling patterns on the Cartesian grid:

Cartesian Subsampling.

Let $0 < r_{\text{acs}} < 1$ be the autocalibration region ratio.

- **Rectilinear:** Achieved by including some and omitting other horizontal (phase encoding direction) lines on the Cartesian grid. For the ACS region we used a number of $r_{\text{acs}} \cdot n_y$ lines.

We employed four distinct rectilinear sampling patterns:

- **Random (Figure 2(a)):** Lines were drawn from the uniform distribution with possible overlap with the ACS lines.
- **Equispaced (Figure 2(b)):** Lines were included with a fixed distancing that satisfied the desired acceleration.
- **Equispaced+ (Figure 2(c)):** Modified equispaced pattern that exploits k -space symmetry as presented in 30.
- **Gaussian 1D (Figure 2(d)):** Lines were drawn from the Gaussian distribution with mean $\mu = \frac{n_y}{2}$ and standard deviation $\sigma = 4 \cdot \sqrt{\mu}$.
- **Variable Density Poisson Disk (VDPD, Figure 2(e)):** Combines both random, and denser center sampling. For our implementation we followed Bridson’s algorithm [28]. Samples were drawn with a density $\frac{1}{1+s|r|}$, i.e., inversely proportional to the k -space radius r and a slope s which were determined by the prescribed acceleration.
- **Gaussian 2D (Figure 2(f)):** Samples were drawn from the Gaussian distribution with mean $\boldsymbol{\mu} = \frac{1}{2}(n_x, n_y)$ and covariance $\boldsymbol{\Sigma} = 4 \cdot \mathbf{I}_2 \cdot \sqrt{\mu}^T$.

Code for VDPD and Gaussian 2D schemes was implemented in Cython for fast and efficient sampling, and for the autocalibration signal we fully-sampled a centered disk with a radius $\frac{n \cdot r_{\text{acs}}}{\pi}$.

Simulated non-Cartesian Subsampling.

To simulate non-Cartesian subsampling, we applied the Circular Cartesian UnderSampling (CIRCUS) [29] technique to produce the following retrospective subsampling patterns for Cartesian data:

- **Radial (Figure 2(g)):** Simulates radial subsampling on the Cartesian grid.
- **Spiral (Figure 2(h)):** Simulates spiral subsampling on the Cartesian grid.

For randomization CIRCUS’ offset parameter as defined in 29, can be set to produce random radial and spiral patterns. CIRCUS was modified to output masks by specifying the acceleration factor. Note that in contrast to the rest of the subsampling patterns above, for the non-Cartesian case we did not sample the ACS region exclusively, as these patterns already fully-sample a great portion of the k -space center. Therefore, for the ACS subsampling mask \mathbf{U}_{acs} we calculated the largest sampled centered disk from \mathbf{U} .

3.2. Deep MRI-reconstruction Model Architecture

3.2.1. The Recurrent Variational Network

To compare and evaluate the aforementioned subsampling techniques we employed a DL-based reconstruction network, namely the Recurrent Variational Network [15] (RecurrentVarNet). The RecurrentVarNet is a DL-based inverse problem solver previously applied on the task of Accelerated MRI Reconstruction [15] with state-of-the-art performance (MC-MRI reconstruction challenge winning solution [31]). It iteratively solves the gradient descent scheme in the measurements domain as portrayed by Eq. 18 using convolutional recurrent neural networks (ConvRNNs) as a regularizer. The RecurrentVarNet takes subsampled multi-coil k -space measurements as input and outputs a prediction of the fully-sampled multi-coil k -space. It comprises three main modules:

• **Recurrent Variational Block (RecurrentVarNet Block).**

The RecurrentVarNet consists of T RecurrentVarNet Blocks, which are the main blocks of the method, each responsible for performing an unrolled gradient descent optimization time-step as in Eq. 18 by replacing \mathcal{H}_{θ_t} with a recurrent unit, denoted as RNN_{θ_t} :

$$\begin{aligned} \mathbf{w}_t, \mathbf{h}_{t+1} &= \text{RNN}_{\theta_{t+1}}(\mathcal{R}_S \circ \mathcal{F}^{-1}(\mathbf{y}_t), \mathbf{h}_t), \\ \mathbf{y}_{t+1} &= \mathbf{y}_t - \alpha_{t+1} \mathbf{U}(\mathbf{y}_t - \tilde{\mathbf{y}}) + \mathcal{F} \circ \mathcal{E}_S(\mathbf{w}_t), \\ \mathbf{y}_0 &= \tilde{\mathbf{y}}, \quad t = 0, \dots, T-1. \end{aligned} \quad (19)$$

Each RNN_{θ_t} is consisted of a convolutional layer (Conv) with a 5×5 kernel followed by n_l cascades of alternating Convs with a 3×3 kernel and convolutional gated recurrent units (ConvGRUs). A rectified linear unit is applied after each Conv excluding the last. RNN_{θ_t} takes as input intermediate quantities of the image projection of the refined k -space $\mathcal{R}_S \circ \mathcal{F}^{-1}(\mathbf{y}_{t-1})$ and the hidden state \mathbf{h}_{t-1} from the previous time-step.

- **Recurrent State Initializer (RSI).** It produces an initialization for the first hidden state \mathbf{h}_0 to be used by RNN_{θ_1} provided as input the SENSE reconstruction of the image projection of \mathbf{y}_0 :

$$\mathbf{h}_0 = \text{RSI}(\mathcal{R}_S \circ \mathcal{F}^{-1}(\mathbf{y}_0)). \quad (20)$$

- **Sensitivity Estimation - Refinement (SER).** It estimates at each iteration the coil sensitivity maps as in Eq. 9, and refines them using a U-Net [32] with trainable parameters ψ denoted as \mathcal{S}_ψ :

$$\mathbf{S} = \text{SER}(\tilde{\mathbf{S}}) : \quad \mathbf{S}^k = \mathcal{S}_\psi(\tilde{\mathbf{S}}^k), \quad k = 1, \dots, n_c. \quad (21)$$

3.3. Experimental Setup

To perform our experiments, we retrospectively subsampled the fully-sampled k -space data by generating subsampling masks as introduced in Section 3.1. We carried out two classes of experiments: scheme-specific and multi-scheme. An overview of our experimental setup is illustrated in Figure 3.

3.3.1. Scheme-specific Setup

To compare the individual subsampling patterns and demonstrate their effect on the quality of DL-based reconstruction, we first performed experiments in a scheme-specific setting: for each dataset-pattern pair we ran individual experiments by training and evaluating (twenty-four) distinct RecurrentVarNets (with the same choice of hyper-parameters as outlined in Section 3.3.4).

3.3.2. Multi-scheme Setup

In the multi-scheme setting, our goal was twofold: Firstly, we aimed to investigate further the effect of each subsampling scheme on the quality of DL-based reconstruction. Secondly, and most importantly, we wanted to assess whether or not a DL-based model trained in a multi-scheme fashion (i.e. training measurements subsampled with multiple subsampling patterns) demonstrated higher reconstruction performance compared to being trained in a scheme-specific fashion (as in Section 3.3.1). Therefore, for each dataset, a RecurrentVarNet was trained on data arbitrarily subsampled with any of the presented subsampling schemes in Section 3.1 and evaluated on all of them.

3.3.3. Subsampling

In both, scheme-specific and multi-scheme settings, throughout the training phase, subsampling masks were generated with an acceleration factor of $R = 2, 4$ or 8 , and were retrospectively applied onto the fully-sampled data. At validation and testing times, data were 2-fold, 4-fold, and 8-fold retrospectively subsampled.

For the Cartesian masks we set $r_{acs} = 0.16, 0.08, 0.04$ for $R = 2, 4, 8$, respectively.

Note that for all experiments, subsampling masks during training were randomly generated to maximize the amount of data that each model saw, while for validation and testing they were predetermined. Additionally, the same subsampling mask was applied to all slices of each volume during validation and testing. It should also be highlighted that all individual coil data of each sample were subsampled with the same subsampling mask as this reflected clinical subsampling.

3.3.4. Model Implementation Details

Hyper-parameter Choice.

For the RecurrentVarNets we used $T = 8$ time-steps. For each RecurrentVarNet Block we used $n_l = 4$ alternating cascades and for the number of filters in each Conv and hidden size in each ConvGRU we chose $n_f = 256$ channels. For the implementation of the RSI and SER modules we picked the same choice of hyper-parameters as the original paper [15].

Training & Optimization Details.

For training and optimization we utilized PyTorch [33]. All components of the Recurrent Variational Network were trained end-to-end and optimization was performed utilizing the Adam algorithm with coefficients $(\beta_1, \beta_2) = (0.9, 0.999)$, stability parameter $\epsilon = 1 \times 10^{-8}$ and no weight decay.

Experiments were performed utilizing NVIDIA RTX A6000, Quadro RTX 8000, or A100 GPUs. Models were trained to convergence with a batch size of 1 slice multi-coil k -space data. The total number of trainable parameters for each model amounted to approximately 27,626k.

Training Loss Function.

At each training iteration each model was fed with subsampled multi-coil k -space measurements $\tilde{\mathbf{y}}$ and produced a prediction \mathbf{y}_T of the fully-sampled reference k -space \mathbf{y} . Loss was computed in the image domain using $\mathbf{x}_T = \text{RSS} \circ \mathcal{F}^{-1}(\mathbf{y}_T)$ as the image prediction and $\hat{\mathbf{x}} = \text{RSS} \circ \mathcal{F}^{-1}(\mathbf{y})$ as the image reference.

As a loss function we used a combination of the mean average error (MAE) loss \mathcal{L}_{MAE} and the structural similarity index measure (SSIM) loss $\mathcal{L}_{\text{SSIM}}$:

$$\begin{aligned} \mathcal{L}(\hat{\mathbf{x}}, \mathbf{x}_T) &= \mathcal{L}_{\text{MAE}}(\hat{\mathbf{x}}, \mathbf{x}_T) + \mathcal{L}_{\text{SSIM}}(\hat{\mathbf{x}}, \mathbf{x}_T) \\ &= \|\hat{\mathbf{x}} - \mathbf{x}_T\|_1 + (1 - \text{SSIM}(\hat{\mathbf{x}}, \mathbf{x}_T)), \end{aligned} \quad (22)$$

where SSIM is defined in Section 3.3.6.

3.3.5. Datasets

To perform our experiments we employed three open source datasets, the fastMRI knee and brain datasets [34] which are to-date the largest publicly available MRI datasets, and the Calgary-Campinas (CC) brain dataset which was released as part of the Multi-Coil MRI Reconstruction Challenge [31]. All datasets consisted of raw k -space volumes of 2D multi-coil, fully-sampled Cartesian k -space data. The acquisition parameters and the splitting ratios we opted for in our experiments are summarized in Table A.1.

3.3.6. Quality Analysis

Metrics. To analyse and compare our results we employed five evaluation metrics commonly used in image processing. Let $\mathbf{u} \in \mathbb{R}^n$ be the reference image and $\mathbf{v} \in \mathbb{R}^n$ the prediction, they are defined as follows:

A) Structural Similarity Index Measure (SSIM)

$$\text{SSIM}(\mathbf{u}, \mathbf{v}) = \frac{1}{M} \sum_{i=1}^M \frac{(2\mu_{\mathbf{u}_i}\mu_{\mathbf{v}_i} + c_1)(2\sigma_{\mathbf{u}_i\mathbf{v}_i} + c_2)}{(\mu_{\mathbf{u}_i}^2 + \mu_{\mathbf{v}_i}^2 + c_1)(\sigma_{\mathbf{u}_i}^2 + \sigma_{\mathbf{v}_i}^2 + c_2)}, \quad (23)$$

where $\mathbf{u}_i, \mathbf{v}_i, i = 1, \dots, M$ are image windows of size $(w_x, w_y) = (7, 7)$ from \mathbf{u} and \mathbf{v} , respectively. The numbers $\mu_{\mathbf{u}_i}, \mu_{\mathbf{v}_i}, \sigma_{\mathbf{u}_i}$ and $\sigma_{\mathbf{v}_i}$ denote the means and standard deviations of each image window and $\sigma_{\mathbf{u}_i\mathbf{v}_i}$ denotes the covariance between \mathbf{u}_i and \mathbf{v}_i . The constants $c_1 = 0.01$ and $c_2 = 0.03$ are used for numerical stability.

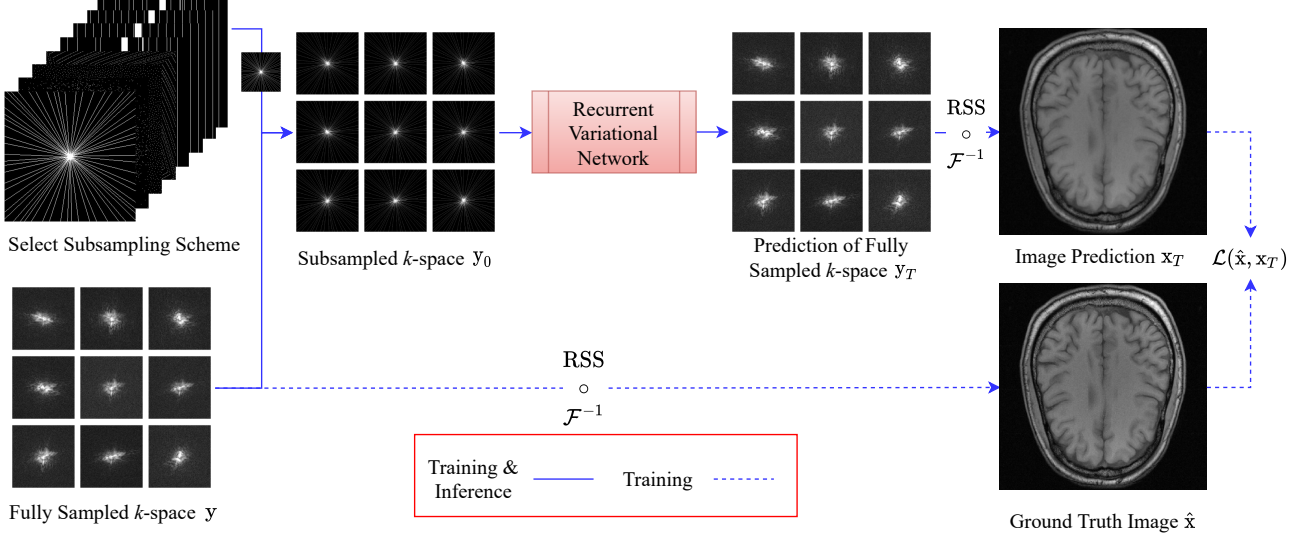


Figure 3: Experiments pipeline: For each subsampling scheme (e.g. here: radial), the fully-sampled multi-coil k -space is retrospectively subsampled and used as input to a RecurrentVarNet, which outputs a prediction of the fully-sampled k -space. The predicted \mathbf{x}_T and ground truth $\hat{\mathbf{x}}$ images are produced by applying the $\text{RSS} \circ \mathcal{F}^{-1}$ operator onto \mathbf{y}_T and \mathbf{y} , respectively. During training, the loss \mathcal{L} is calculated using \mathbf{x}_T and $\hat{\mathbf{x}}$.

B) Peak Signal-to-Noise Ratio (pSNR)

$$\text{pSNR}(\mathbf{u}, \mathbf{v}) = 20 \log_{10} \left(\frac{\max(\mathbf{u})}{\sqrt{\frac{1}{n} \sum_i^n (\mathbf{u}_i - \mathbf{v}_i)^2}} \right). \quad (24)$$

C) Signal-to-Noise Ratio (SNR)

$$\text{SNR}(\mathbf{u}, \mathbf{v}) = 10 \log_{10} \left(\frac{\sum_i^n \mathbf{u}_i^2}{\sum_i^n (\mathbf{u}_i - \mathbf{v}_i)^2} \right). \quad (25)$$

D) High Frequency Error Norm (HFEN)

$$\text{HFEN}_C(\mathbf{u}, \mathbf{v}) = \frac{\|\text{LoG}(\mathbf{u}) - \text{LoG}(\mathbf{v})\|_C}{\|\text{LoG}(\mathbf{v})\|_C}, \quad (26)$$

where where LoG is a Laplacian-of-Gaussian filter [35] with kernel of size 15×15 and with a standard deviation of 2.5, and $C = 1$ or 2 .

E) Normalized Mean Squared Error (NMSE)

$$\text{NMSE}(\mathbf{u}, \mathbf{v}) = \frac{\|\mathbf{u} - \mathbf{v}\|_2^2}{\|\mathbf{u}\|_2^2} = \frac{\sum_i^n (\mathbf{u}_i - \mathbf{v}_i)^2}{\sum_i^n \mathbf{u}_i^2}. \quad (27)$$

Note that the higher the computed SSIM, SNR, and pSNR values, the higher the quality of the reconstruction is. Conversely, for the HFEN and NMSE values, the lower they are, the higher the quality of the reconstruction is. Reported values for SSIM and NMSE are multiplied by 100 and 1000, respectively.

3.3.7. Significance Tests

To perform significance tests we used the Almost Stochastic Order (ASO) test [36, 37] with a 95% confidence level ($\alpha = 0.05$). Each ASO test outputs a violation error ϵ_{\min} which denotes the degree to which the hypothesis that "method A is always better than method B" is being violated. If $\epsilon_{\min} < 0.5$ one can claim that A is better than B, and otherwise if $\epsilon_{\min} \geq 0.5$.

3.3.8. Robustness to Model Choice Experiments

To ensure that the findings presented in Section Section 4 are not reliant on the choice of the model architecture, we conducted additional experiments using an alternative advanced deep-MRI reconstruction network known as the Recurrent Inference Machine (RIM). Specifically, we replicated the scheme-specific experiments on the CC dataset by substituting the RecurrentVarNet with a RIM. The hyper-parameter settings for each RIM were consistent with those employed in the study in [17].

4. Results

To obtain our results, data preparation, retrospective subsampling generation, and model training we used the Deep Image Reconstruction Toolkit (DIRECT) [38].

4.1. Scheme-specific Setup Results

Figure 4 illustrates the quantitative metrics computed on the test sets in the form of violin-plots. The average metrics are reported in Table A.2. Additionally, for visual assessment, in Figure 5, Figure 6, and Figure A.1 we present example reconstructions of a test sample from each dataset using all methods along with ground truths and the retrospective subsampling mask used in each scenario.

4.1.1. Cartesian

Rectilinear. Figure 4 indicates that all models trained on rectilinearly subsampled measurements achieved comparable results when evaluated on the test sets subsampled with the respective rectilinear schemes. Moreover, although Gaussian 1D subsampling outperformed the rest of the rectilinear schemes in the case of both fastMRI datasets, the opposite was noted in the case of the CC dataset. This is also visible by the example

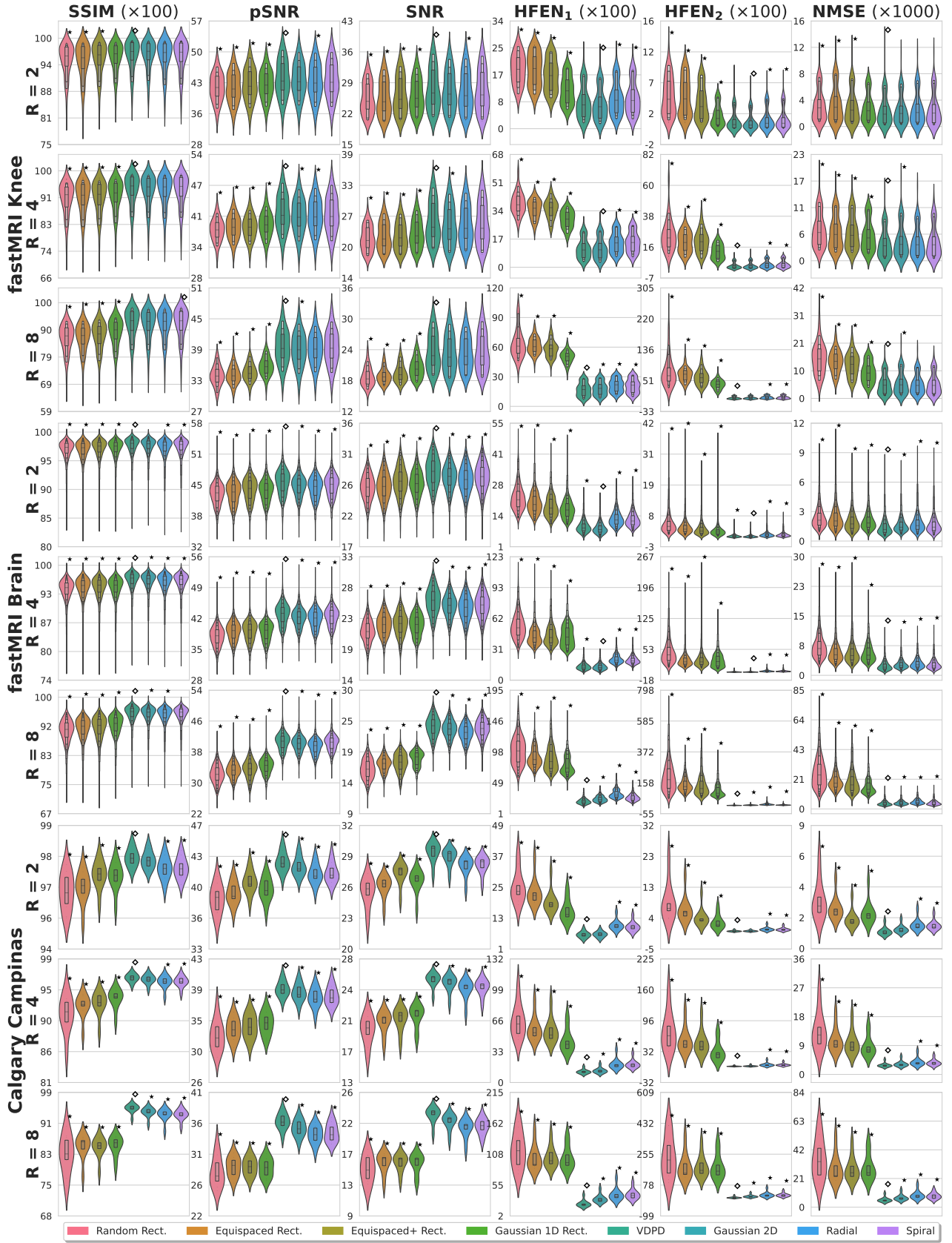


Figure 4: Scheme-specific experiments quantitative results on the test sets. For each dataset-subsampling scheme pair a distinct model was trained (in total 24 models). For each dataset-acceleration-metric combination, pair-wise ASO significance tests were performed between the average best performing, denoted by \diamond , and the rest schemes. The symbol \star indicates that VDPD was found to be significantly better. Average metrics are reported in Table A.2.

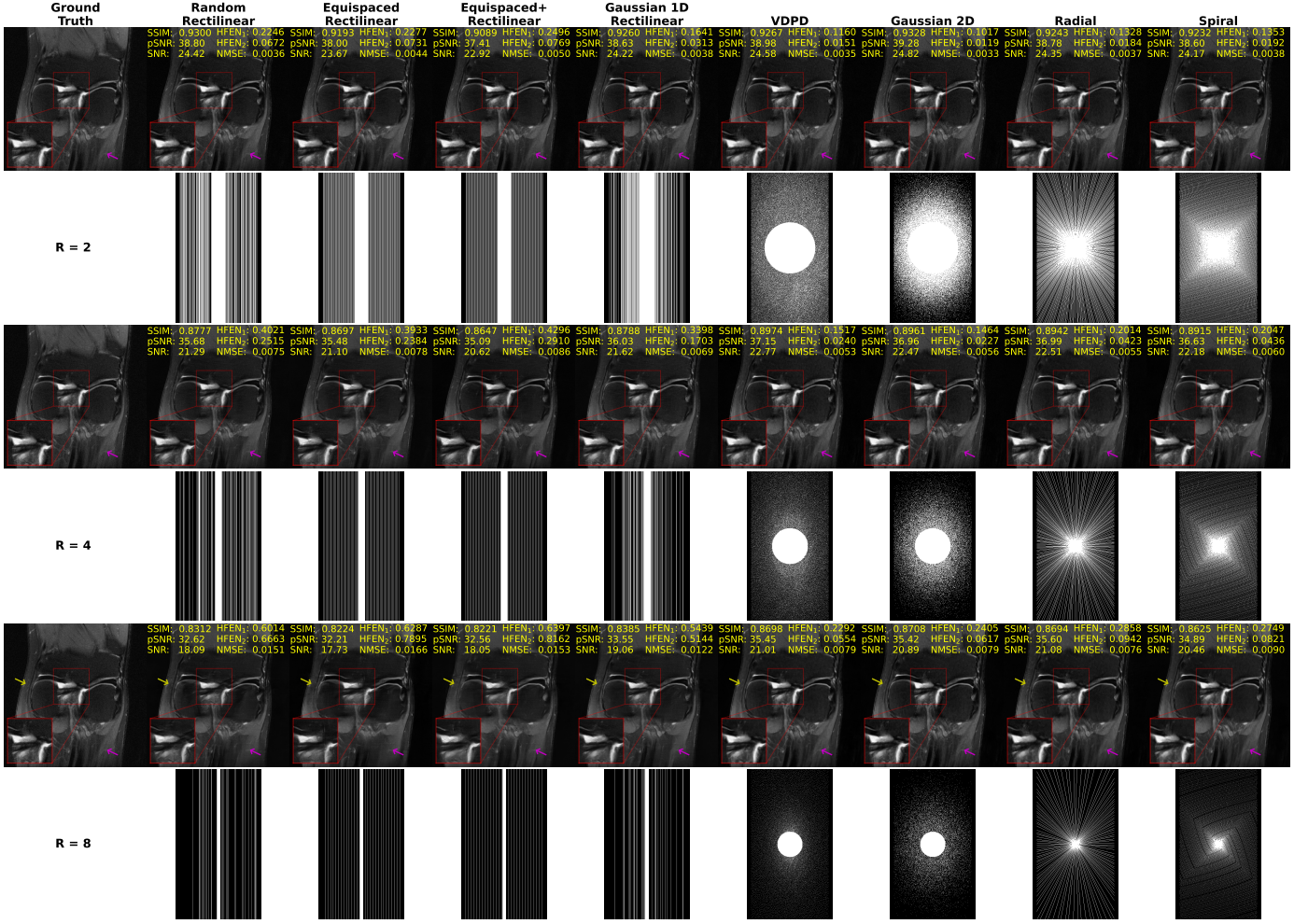


Figure 5: Representative reconstruction of a sample from the fastMRI knee test set obtained from the scheme-specific experiments. For the ground truth image the RSS method was applied on the fully sampled k -space. For each subsampling scheme, we retrospectively applied subsampling masks as shown in rows 2, 4, 6 (with accelerations factors of 2, 4, 8, respectively) onto the fully sampled k -space. Rows 1, 3, 5 illustrate the center-cropped RSS-reconstructed k -space output from each model. Quantitative metrics against the ground truth are inscribed on the top left of each reconstruction.

reconstructions in Figures 5, 6, and Figure A.1, especially for 8-fold acceleration.

Non-Rectilinear. As Figure 4 and Table A.2 indicate, models trained on data subsampled with either VDPD or Gaussian 2D schemes were the best-performing models when evaluated on the respective data. Additionally, they produced reconstructions with the higher average SSIM, pSNR, and SNR and lower HFEN and NMSE values for all combinations of datasets and acceleration factors.

4.1.2. Non-Cartesian

As shown in Figure 4 and Table A.2, models trained and evaluated on simulated non-Cartesian (radially and spirally) subsampled data yielded similar performance to Cartesian non-rectilinear schemes. In general, spiral schemes outperformed radial schemes for all combinations of datasets and acceleration factors, though the difference in performance was minor.

4.1.3. Comparisons

Considering Figure 4, models trained on non-rectilinearly subsampled data, produced reconstructions of higher fidelity when evaluated on the respective test sets in comparison to models trained and evaluated on rectilinearly subsampled data for all datasets and acceleration factors. Models trained with VDPD or Gaussian 2D -subsampled k -spaces obtained the best average quantitative evaluation results.

As can be seen from Figures 5, 6, and A.1, for high acceleration factors (4 or 8) models trained on rectilinear schemes reconstructed images with more errors and artifacts, compared to non-Cartesian or non-rectilinear schemes. However, for $R = 2$ all models performed similarly.

4.2. Multi-scheme Setup Results

Figure 7 reports the quantitative evaluation results on the test sets in the multi-scheme setup and Table A.3 the corresponding average metrics. We observe that, similarly to the results of Section 4.1, reconstructions of non-rectilinearly subsampled measurements produced better quantitative results compared to

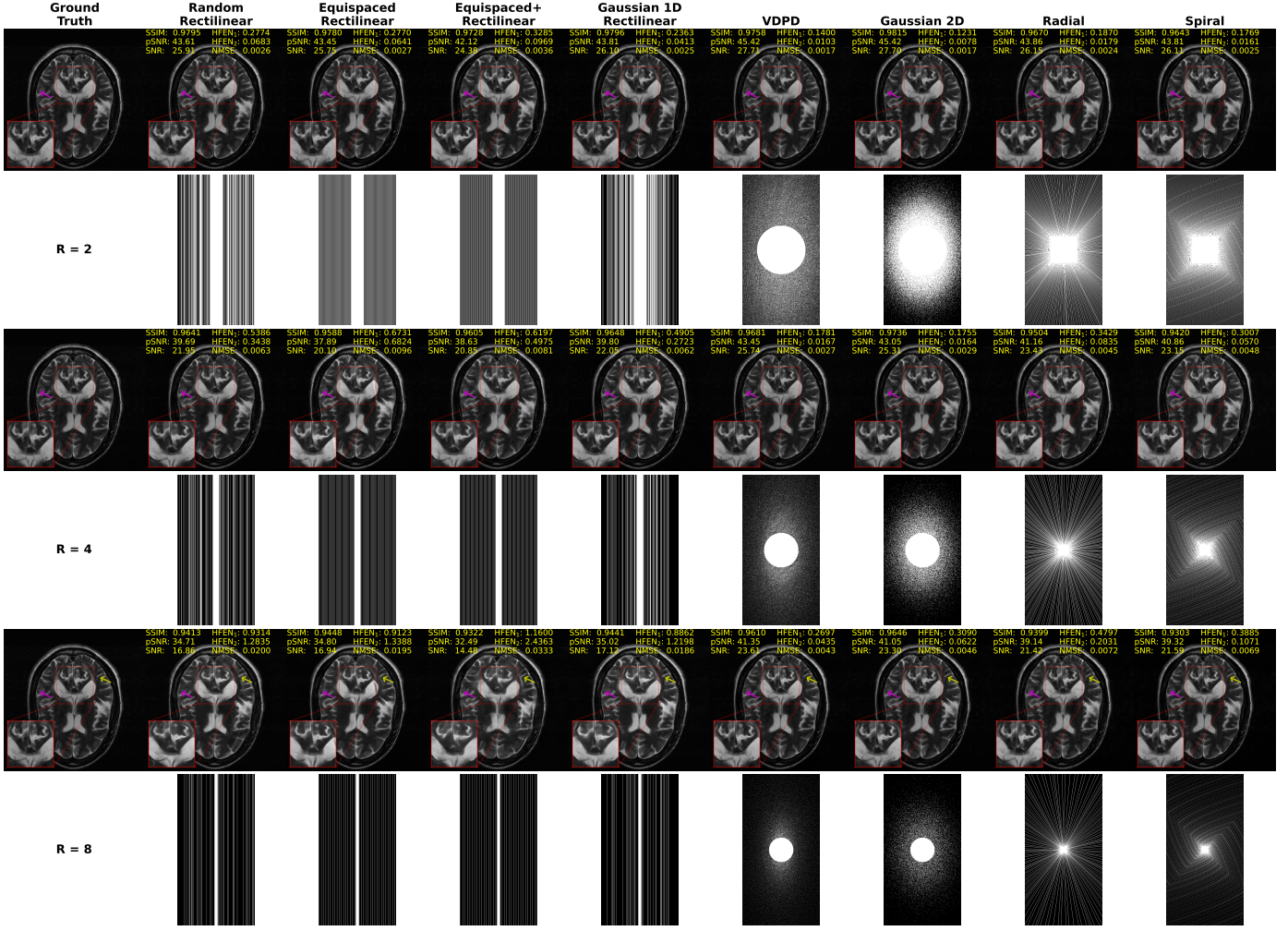


Figure 6: Representative reconstruction of a T2-weighted sample from the fastMRI brain test set obtained from the scheme-specific experiments. For the ground truth image the RSS method was applied on the fully sampled k -space. For each subsampling scheme, we retrospectively applied subsampling masks as shown in rows 2, 4, 6 (with accelerations factors of 2, 4, 8, respectively) onto the fully sampled k -space. Rows 1, 3, 5 illustrate the center-cropped RSS-reconstructed k -space output from each model. Quantitative metrics against the ground truth are inscribed on the top left of each reconstruction.

reconstructions of rectilinearly subsampled data. In addition, VDPD and Gaussian 2D-subsampled reconstructions were the highest performing on average.

For further investigation, in Figure A.2, utilizing the results reported in Figure 7, we calculated the per-case difference in evaluation metrics change for each pattern using as reference the results obtained in the scheme-specific setup (Figure 4). We also report the average differences for rectilinear and non-rectilinear patterns in Table 1. Interestingly, models trained in the multi-scheme setting exemplified superior performance when evaluated on measurements subsampled with rectilinear schemes compared against the models trained on individual schemes when evaluated on the same data. In particular, in the case of rectilinear schemes, noticeable improvements (SSIM/pSNR/SNR increase, HFEN/NMSE decrease) on the reconstruction performance were remarked for all datasets and acceleration factors, whilst for non-rectilinear patterns no change or minor deterioration was observed.

In Figures 8 and A.3 we show representative reconstructions

predicted from rectilinearly-subsampled data obtained from both, the scheme-specific and multi-scheme setups. By visual investigation, we notice that the latter reconstructed images were more faithful.

4.3. Robustness to Model Choice Results

The quantitative metrics for our experiments using the Recurrent Inference Machine (RIM) are shown in Figure A.4 and Table A.4. These results are on par with the findings of our original experiments, indicating that our conclusions remain valid regardless of the specific deep learning architecture employed.

5. Discussion

In this work we investigated and compared various retrospective k -space subsampling patterns and we experimentally studied their effect on the quality of DL-based reconstructions. Since the data we utilized in our studies were Cartesian fully-sampled acquisitions, we retrospectively generated

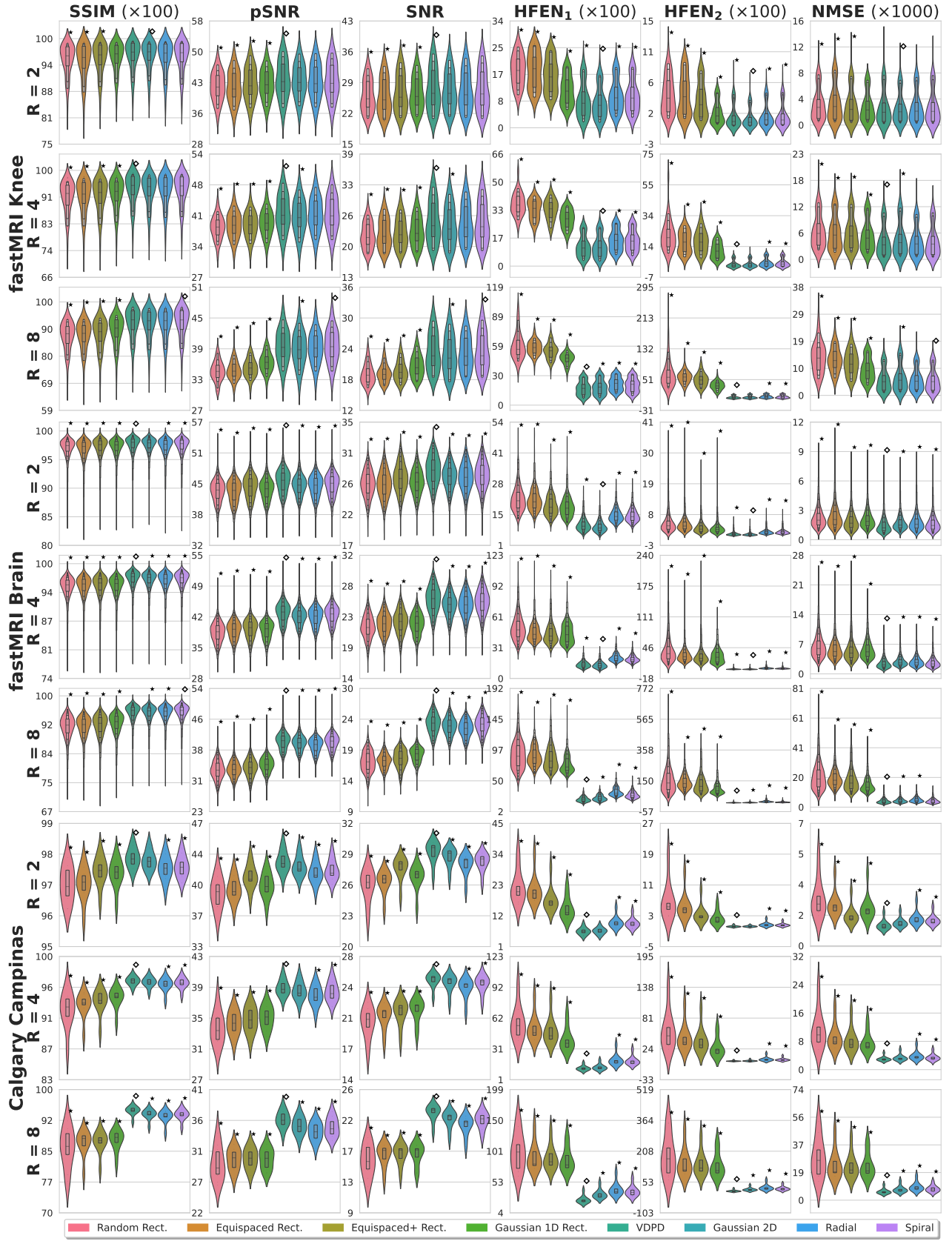


Figure 7: Multi-scheme experiments quantitative results on the test sets. A model was trained for each dataset on data subsampled by any of the presented schemes. For each dataset-acceleration-metric combination, pair-wise ASO significance tests were performed between the average best performing (denoted by ◊) and the rest schemes. The symbol ★ indicates that the best scheme was found to be significantly better ($\epsilon_{\min} < 0.5$). Average metrics are reported in Table A.3.

Table 1: Scheme-specific-Multi-scheme experiments performance average percentage difference. Percentages were acquired by averaging the per-case differences (as calculated and illustrated in Figure A.2) for all dataset-scheme type (rectilinear or non-rectilinear) combinations.

Dataset	Acceleration Factor	Rectilinear							Non-rectilinear				
		SSIM	pSNR	SNR	HFEN _{L1}	HFEN _{L2}	NMSE	SSIM	pSNR	SNR	HFEN _{L1}	HFEN _{L2}	NMSE
fastMRI Knee	2	0.1%	0.5%	0.7%	-2.7%	-5.3%	-0.7%	-0.0%	-0.3%	-0.7%	4.4%	7.1%	5.6%
	4	0.3%	0.7%	0.9%	-4.3%	-11.0%	-3.1%	-0.0%	-0.2%	-0.7%	2.2%	4.8%	4.2%
	8	0.7%	1.4%	2.1%	-6.2%	-15.4%	-9.5%	0.0%	-0.1%	-0.5%	-0.2%	0.3%	3.0%
fastMRI Brain	2	0.0%	0.3%	0.4%	-0.0%	-0.6%	-2.6%	-0.0%	-0.2%	-0.3%	6.2%	13.2%	1.6%
	4	0.1%	0.3%	0.4%	-0.5%	-1.9%	-2.7%	-0.0%	-0.1%	-0.0%	1.3%	3.4%	0.5%
	8	0.4%	1.2%	2.1%	-4.2%	-9.8%	-8.5%	0.0%	0.1%	0.3%	2.6%	11.3%	-0.9%
Calgary Campinas	2	0.3%	1.5%	2.2%	-9.1%	-19.1%	-12.9%	0.0%	0.1%	0.1%	-1.2%	-4.7%	-0.8%
	4	0.9%	2.2%	3.5%	-10.6%	-20.1%	-14.8%	0.0%	-0.1%	-0.1%	0.9%	2.2%	0.7%
	8	2.3%	3.1%	5.7%	-12.2%	-22.1%	-17.8%	-0.0%	-0.2%	-0.3%	3.1%	6.0%	2.0%

subsampling masks on the Cartesian grid as demonstrated in Section 3.1, simulating prospective Cartesian or non-Cartesian accelerated acquisitions. In particular, we generated four Cartesian rectilinear schemes (random, equispaced, equispaced with symmetry correction, Gaussian 1D), non-rectilinear Cartesian schemes (Variable Density Poisson-disk and Gaussian 2D), and simulated (non-Cartesian) radial and spiral schemes.

Our experiments consisted of utilizing a state-of-the-art DL-based accelerated MRI reconstruction method - the Recurrent Variational Network. Although choosing the optimal DL-based MRI reconstruction algorithm was out of the scope of this project, it is important to note that other DL-based models do exist with similar performance. However, the RecurrentVarNet was selected due to its proven ability to produce high-quality reconstructions and its superior performance compared to other models in the field. Additionally, to demonstrate that the results were not model-dependent, the scheme-specific experiments on the CC dataset were repeated using the RIM model which produced on-par results.

Experiments were performed under two setups: scheme-specific and multi-scheme setups. In the scheme-specific settings, we trained individual models on data retrospectively subsampled with individual subsampling patterns applying various acceleration factors. Quantitative and qualitative results demonstrated that the models trained on conventional rectilinear schemes, compared to the other schemes, produced lower quality reconstructions with more artifacts especially for higher acceleration factors (4 or 8). This can be attributed to the fact that non-rectilinear Cartesian such as the VDPD or the Gaussian 2D, and non-Cartesian patterns such as the radial or spiral, allow for more incoherent sampling. This means that these schemes result in a more randomized and less correlated distribution of samples, reducing the dependence of the reconstruction quality on any specific pattern of missing data. Additionally, these schemes allow for center oversampling, which contains information such as contrast and the general shape of the reconstruction.

In the multi-scheme setup, unified models were trained on all data subsampled by all types of subsampling patterns. Results showed that non-rectilinearly subsampled data reconstructions were of superior quality compared to rectilinear reconstructions, aligning with the findings from the scheme-specific experiments. Despite this, the reconstruction performance for rectilinearly subsampled measurements improved notably com-

pared to the scheme-specific setup (see Table 1 and Figure A.2). Additionally, the violin-plots in Figure 4 and Figure 7 show that in both setups for most dataset-metric-acceleration combinations quantitative results for the four rectilinear and the four non-rectilinear schemes formed similar metric distributions and were with similar numbers of outliers, suggesting that results were also case-dependent.

Even though comparing prospective acquisition speeds was out of the scope of this project, we provide a brief discussion. While the reconstruction performance of Cartesian rectilinearly subsampled data was inferior to Cartesian non-rectilinear, someone could argue about the trade-off between acquisition speed and quality, as MRI scanners can perform rectilinear sampling in fast acquisition times [4], while strategies such as VDPD or Gaussian 2D can be slower due to physical limitations. For instance, in the prospective case these strategies may require large gradient switches in the MRI scanner due to the enlarged k -space spacing which can cause extended times due to hardware constraints, whilst in the retrospective settings, efficient algorithms are used to pick the samples.

On the other hand, our results indicated that synthesized radial or spiral schemes on the Cartesian grid using the CIRCUS method provided similar performance to VDPD and Gaussian 2D schemes. In the original paper [29], the authors state that their method improved sampling efficiency over VDPD while maintaining the reconstruction performance in the prospective case.

However, prospective non-Cartesian sampling trajectories do not sample on a Cartesian grid, and therefore samples closer to the center are more densely placed, and more scattered far off. As a result of this non-uniformity, the application of the (inverse) non-uniform FFT (NUFFT) [39] is required, which includes a (inverse) gridding process [40], and possibly accumulating additional computation times.

The main limitation of this study is the fact that experiments were performed retrospectively using fully sampled data. It is important to note that comparing Cartesian and non-Cartesian data acquired prospectively could introduce confounding factors such as different contrasts, potentially leading to unfair comparisons. Nevertheless, the retrospective approach allowed us to directly compare the performance of DL-based reconstructions on various subsampling patterns, thus enabling a clearer understanding of their relative strengths and limitations.

Future studies could explore repeating our experiments us-

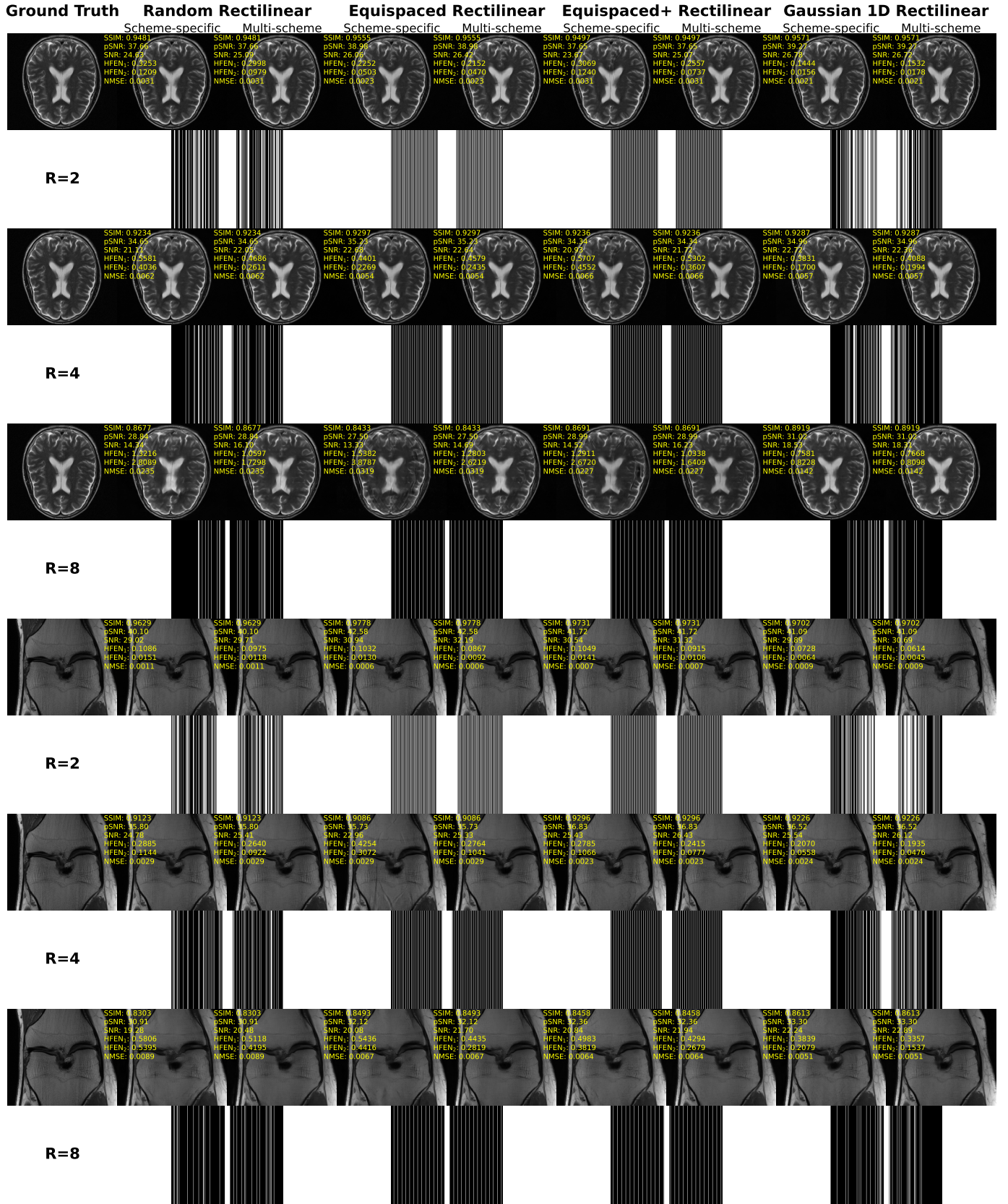


Figure 8: Scheme-specific vs multi-scheme setup visual comparison: Representative reconstructions of two samples from the fastMRI datasets. Measurements were subsampled with the four rectilinear schemes for three acceleration factors.

ing prospectively subsampled data with the different schemes we employed in this study, including non-Cartesian acquisition, in order to determine the extend to which our findings hold true in prospective settings. Additionally, an alternative approach would be to generate prospective non-Cartesian acquisitions from the available Cartesian fully sampled data. To that end it will be necessary to apply one of the methods discussed in the previous paragraph to handle non-Cartesian data in order to incorporate it into our deep learning pipeline and match the multi-scheme framework used in this study.

Another limitation worth considering is that while in our experiments we retrospectively acquired the ACS region and subsampled measurements from the same fully-sampled k-space, this may not be the case in the prospective scenario, as the ACS region may be sampled at different timings. This variation in the sampling of the ACS region may affect the contrast of the reconstructed image, and therefore warrants further investigation.

6. Conclusion

In summary, our study sheds light on the impact of k -space subsampling patterns on DL-based MRI reconstructions. By comparing rectilinear and non-rectilinear Cartesian patterns, as well as pseudo-non-Cartesian trajectories, we demonstrated that DL-based reconstructions perform more robustly and accurately trained with non-rectilinearly subsampled data, allowing for higher acceleration factors. The evaluations conducted using the six quality metrics (SSIM, pSNR, SNR, HFEN₁, HFEN₂, NMSE) consistently showed that non-rectilinear schemes outperformed rectilinear schemes in terms of reconstruction quality. Our work provides a foundation for future research in exploring DL-based MRI reconstructions with different sampling schemes and encourages further investigation into advanced non-Cartesian trajectories.

References

- [1] D. Donoho, Compressed sensing, *IEEE Transactions on Information Theory* 52 (4) (2006) 1289–1306. doi:10.1109/TIT.2006.871582.
- [2] E. J. Candès, J. K. Romberg, T. Tao, Stable signal recovery from incomplete and inaccurate measurements, *Communications on Pure and Applied Mathematics* 59 (8) (2006) 1207–1223. arXiv:https://onlinelibrary.wiley.com/doi/pdf/10.1002/cpa.20124, doi:https://doi.org/10.1002/cpa.20124. URL https://onlinelibrary.wiley.com/doi/abs/10.1002/cpa.20124
- [3] E. Candès, J. Romberg, T. Tao, Robust uncertainty principles: exact signal reconstruction from highly incomplete frequency information, *IEEE Transactions on Information Theory* 52 (2) (2006) 489–509. doi:10.1109/TIT.2005.862083.
- [4] M. Lustig, D. Donoho, J. M. Pauly, Sparse mri: The application of compressed sensing for rapid mr imaging, *Magnetic Resonance in Medicine* 58 (6) (2007) 1182–1195. arXiv:https://onlinelibrary.wiley.com/doi/pdf/10.1002/mrm.21391, doi:https://doi.org/10.1002/mrm.21391. URL https://onlinelibrary.wiley.com/doi/abs/10.1002/mrm.21391
- [5] C. Shannon, Communication in the presence of noise, *Proceedings of the IRE* 37 (1) (1949) 10–21. doi:10.1109/JRPROC.1949.232969.
- [6] S. Ma, W. Yin, Y. Zhang, A. Chakraborty, An efficient algorithm for compressed mr imaging using total variation and wavelets, in: 2008 IEEE Conference on Computer Vision and Pattern Recognition, 2008, pp. 1–8. doi:10.1109/CVPR.2008.4587391.
- [7] M. A. Griswold, P. M. Jakob, R. M. Heidemann, M. Nittka, V. Jellus, J. Wang, B. Kiefer, A. Haase, Generalized autocalibrating partially parallel acquisitions (GRAPPA), *Magnetic Resonance in Medicine* 47 (6) (2002) 1202–1210. doi:10.1002/mrm.10171. URL https://doi.org/10.1002%2Fmrm.10171
- [8] K. P. Pruessmann, Encoding and reconstruction in parallel mri, *NMR in Biomedicine* 19 (3) (2006) 288–299. arXiv:https://analyticalsciencejournals.onlinelibrary.wiley.com/doi/pdf/10.1002/nbm.1042, doi:https://doi.org/10.1002/nbm.1042. URL https://analyticalsciencejournals.onlinelibrary.wiley.com/doi/abs/10.1002/nbm.1042
- [9] M. Lustig, J. M. Pauly, Spirit: Iterative self-consistent parallel imaging reconstruction from arbitrary k-space, *Magnetic Resonance in Medicine* 64 (2) (2010) 457–471. doi:10.1002/mrm.22428. URL https://doi.org/10.1002%2Fmrm.22428
- [10] K. Hammernik, T. Klatzer, E. Kobler, M. P. Recht, D. K. Sodickson, T. Pock, F. Knoll, Learning a variational network for reconstruction of accelerated mri data, *Magnetic Resonance in Medicine* 79 (6) (2018) 3055–3071. arXiv:https://onlinelibrary.wiley.com/doi/pdf/10.1002/mrm.26977, doi:https://doi.org/10.1002/mrm.26977. URL https://onlinelibrary.wiley.com/doi/abs/10.1002/mrm.26977
- [11] T. Eo, Y. Jun, T. Kim, J. Jang, H.-J. Lee, D. Hwang, Kiki-net: cross-domain convolutional neural networks for reconstructing undersampled magnetic resonance images, *Magnetic Resonance in Medicine* 80 (5) (2018) 2188–2201. doi:10.1002/mrm.27201. URL https://doi.org/10.1002%2Fmrm.27201
- [12] K. Lønning, P. Putzky, J.-J. Sonke, L. Reneman, M. W. Caan, M. Welling, Recurrent inference machines for reconstructing heterogeneous mri data, *Medical Image Analysis* 53 (2019) 64–78. doi:https://doi.org/10.1016/j.media.2019.01.005. URL https://www.sciencedirect.com/science/article/pii/S1361841518306078
- [13] A. Sriram, J. Zbontar, T. Murrell, C. L. Zitnick, A. Defazio, D. K. Sodickson, Grappanet: Combining parallel imaging with deep learning for multi-coil mri reconstruction, in: *Proceedings of the IEEE/CVF Conference on Computer Vision and Pattern Recognition (CVPR)*, 2020.
- [14] R. Souza, M. Bento, N. Nogovitsyn, K. J. Chung, W. Loos, R. M. Lebel, R. Frayne, Dual-domain cascade of u-nets for multi-channel magnetic resonance image reconstruction, *Magnetic Resonance Imaging* 71 (2020) 140–153. doi:10.1016/j.mri.2020.06.002. URL https://doi.org/10.1016%2Fj.mri.2020.06.002
- [15] G. Yiasemis, J.-J. Sonke, C. Sánchez, J. Teuwen, Recurrent variational network: A deep learning inverse problem solver applied to the task of accelerated mri reconstruction, in: *Proceedings of the IEEE/CVF Conference on Computer Vision and Pattern Recognition (CVPR)*, 2022, pp. 732–741.
- [16] L. Feng, R. Grimm, K. T. Block, H. Chandarana, S. Kim, J. Xu, L. Axel, D. K. Sodickson, R. Otazo, Golden-angle radial sparse parallel MRI: combination of compressed sensing, parallel imaging, and golden-angle radial sampling for fast and flexible dynamic volumetric MRI, *Magn. Reson. Med.* 72 (3) (2014) 707–717.
- [17] G. Yiasemis, C. Zhang, C. I. Sánchez, J.-J. Sonke, J. Teuwen, Deep MRI reconstruction with radial subsampling, in: W. Zhao, L. Yu (Eds.), *Medical Imaging 2022: Physics of Medical Imaging*, SPIE, 2022. doi:10.1117/12.2609876. URL https://doi.org/10.1117%2F12.2609876
- [18] K. P. Pruessmann, M. Weiger, M. B. Scheidegger, P. Boesiger, Sense: Sensitivity encoding for fast mri, *Magnetic Resonance in Medicine* 42 (5) (1999) 952–962. arXiv:https://onlinelibrary.wiley.com/doi/pdf/10.1002/10.1002/(SICI)1522-2594(199911)42:5<952::AID-MRM16>3.0.CO;2-S, doi:https://doi.org/10.1002/(SICI)1522-2594(199911)42:5<952::AID-MRM16>3.0.CO;2-S. URL https://onlinelibrary.wiley.com/doi/pdf/10.

- 1002/10.1002/(SICI)1522-2594(199911)42:5<952::AID-MRM16>3.0.CO;2-S
- [19] A. Majumdar, R. K. Ward, Iterative estimation of mri sensitivity maps and image based on sense reconstruction method (isense), *Concepts in Magnetic Resonance Part A* 40A (6) (2012) 269–280. [arXiv:https://onlinelibrary.wiley.com/doi/pdf/10.1002/cmr.a.21244](https://onlinelibrary.wiley.com/doi/pdf/10.1002/cmr.a.21244), doi:<https://doi.org/10.1002/cmr.a.21244>. URL <https://onlinelibrary.wiley.com/doi/abs/10.1002/cmr.a.21244>
- [20] M. Uecker, P. Lai, M. J. Murphy, P. Virtue, M. Elad, J. M. Pauly, S. S. Vasanawala, M. Lustig, ESPIRiT—an eigenvalue approach to autocalibrating parallel MRI: where SENSE meets GRAPPA, *Magn. Reson. Med.* 71 (3) (2014) 990–1001.
- [21] A. Sriram, J. Zbontar, T. Murrell, A. Defazio, C. L. Zitnick, N. Yakubova, F. Knoll, P. Johnson, End-to-end variational networks for accelerated mri reconstruction, in: A. L. Martel, P. Abolmaesumi, D. Stoyanov, D. Mateus, M. A. Zuluaga, S. K. Zhou, D. Racoceanu, L. Joskowicz (Eds.), *Medical Image Computing and Computer Assisted Intervention – MICCAI 2020*, Springer International Publishing, Cham, 2020, pp. 64–73.
- [22] X. Liu, W. Xu, X. Ye, The ill-posed problem and regularization in parallel magnetic resonance imaging, in: 2009 3rd International Conference on Bioinformatics and Biomedical Engineering, 2009, pp. 1–4. doi:10.1109/ICBBE.2009.5163622.
- [23] M. Uecker, Parallel magnetic resonance imaging, *arXiv*, 2015. doi:10.48550/ARXIV.1501.06209. URL <https://arxiv.org/abs/1501.06209>
- [24] D. K. Sodickson, C. A. McKenzie, A generalized approach to parallel magnetic resonance imaging, *Medical Physics* 28 (8) (2001) 1629–1643. doi:10.1118/1.1386778. URL <https://doi.org/10.1118/2F1.1386778>
- [25] E. Piccolomini, F. Zama, G. Zanghirati, A. Formiconi, Regularization methods in dynamic mri, *Applied Mathematics and Computation* 132 (2) (2002) 325–339. doi:[https://doi.org/10.1016/S0096-3003\(01\)00196-5](https://doi.org/10.1016/S0096-3003(01)00196-5). URL <https://www.sciencedirect.com/science/article/pii/S0096300301001965>
- [26] F.-H. Lin, K. K. Kwong, J. W. Belliveau, L. L. Wald, Parallel imaging reconstruction using automatic regularization, *Magnetic Resonance in Medicine* 51 (3) (2004) 559–567. doi:10.1002/mrm.10718. URL <https://doi.org/10.1002/2Fmrm.10718>
- [27] F. Knoll, C. Clason, K. Bredies, M. Uecker, R. Stollberger, Parallel imaging with nonlinear reconstruction using variational penalties, *Magnetic Resonance in Medicine* 67 (1) (2012) 34–41. [arXiv:https://onlinelibrary.wiley.com/doi/pdf/10.1002/mrm.22964](https://onlinelibrary.wiley.com/doi/pdf/10.1002/mrm.22964), doi:<https://doi.org/10.1002/mrm.22964>. URL <https://onlinelibrary.wiley.com/doi/abs/10.1002/mrm.22964>
- [28] R. Bridson, Fast poisson disk sampling in arbitrary dimensions, in: *ACM SIGGRAPH 2007 Sketches, SIGGRAPH '07*, Association for Computing Machinery, New York, NY, USA, 2007, p. 22–es. doi:10.1145/1278780.1278807. URL <https://doi.org/10.1145/1278780.1278807>
- [29] J. Liu, D. Saloner, Accelerated mri with circular cartesian undersampling (circus): a variable density cartesian sampling strategy for compressed sensing and parallel imaging, *Quantitative Imaging in Medicine and Surgery* 4 (1) (2014). doi:10.3978/j.issn.2223-4292.2014.02.01. URL <https://qims.amegroups.com/article/view/3439>
- [30] A. Defazio, Offset sampling improves deep learning based accelerated mri reconstructions by exploiting symmetry (2019). doi:10.48550/ARXIV.1912.01101. URL <https://arxiv.org/abs/1912.01101>
- [31] Y. Beauferris, J. Teuwen, D. Karkalousos, N. Moriakov, M. Caan, G. Yiasemis, L. Rodrigues, A. Lopes, H. Pedrini, L. Rittner, M. Dannecker, V. Studenyak, F. Gröger, D. Vyas, S. Faghih-Roohi, A. K. Jethi, J. C. Raju, M. Sivaprakasam, M. Lasby, N. Nogovitsyn, W. Loos, R. Frayne, R. Souza, Multi-coil MRI reconstruction challenge—assessing brain MRI reconstruction models and their generalizability to varying coil configurations, *Frontiers in Neuroscience* 16 (jul 2022). doi:10.3389/fnins.2022.919186. URL <https://doi.org/10.3389/2Ffnins.2022.919186>
- [32] O. Ronneberger, P. Fischer, T. Brox, U-net: Convolutional networks for biomedical image segmentation, in: *Lecture Notes in Computer Science*, Springer International Publishing, 2015, pp. 234–241. doi:10.1007/978-3-319-24574-4_28. URL https://doi.org/10.1007/978-3-319-24574-4_28
- [33] A. Paszke, S. Gross, F. Massa, A. Lerer, J. Bradbury, G. Chanan, T. Killeen, Z. Lin, N. Gimelshein, L. Antiga, A. Desmaison, A. Kopf, E. Yang, Z. DeVito, M. Raison, A. Tejani, S. Chilamkurthy, B. Steiner, L. Fang, J. Bai, S. Chintala, Pytorch: An imperative style, high-performance deep learning library, in: H. Wallach, H. Larochelle, A. Beygelzimer, F. d'Alché-Buc, E. Fox, R. Garnett (Eds.), *Advances in Neural Information Processing Systems*, Vol. 32, Curran Associates, Inc., 2019. URL https://proceedings.neurips.cc/paper_files/paper/2019/file/bdbca288fee7f92f2bfa9f7012727740-Paper.pdf
- [34] J. Zbontar, F. Knoll, A. Sriram, T. Murrell, Z. Huang, M. J. Muckley, A. Defazio, R. Stern, P. Johnson, M. Bruno, M. Parente, K. J. Geras, J. Katsnelson, H. Chandarana, Z. Zhang, M. Drozdal, A. Romero, M. Rabbat, P. Vincent, N. Yakubova, J. Pinkerton, D. Wang, E. Owens, C. L. Zitnick, M. P. Recht, D. K. Sodickson, Y. W. Lui, fastmri: An open dataset and benchmarks for accelerated mri (2018). doi:10.48550/ARXIV.1811.08839. URL <https://arxiv.org/abs/1811.08839>
- [35] S. Ravishanker, Y. Bresler, Mr image reconstruction from highly undersampled k-space data by dictionary learning, *IEEE Transactions on Medical Imaging* 30 (5) (2011) 1028–1041. doi:10.1109/TMI.2010.2090538.
- [36] R. Dror, S. Shlomov, R. Reichart, Deep dominance - how to properly compare deep neural models, in: *Proceedings of the 57th Annual Meeting of the Association for Computational Linguistics*, Association for Computational Linguistics, Florence, Italy, 2019, pp. 2773–2785. doi:10.18653/v1/P19-1266. URL <https://aclanthology.org/P19-1266>
- [37] D. Ulmer, C. Hardmeier, J. Frellsen, deep-significance-easy and meaningful statistical significance testing in the age of neural networks, *arXiv preprint arXiv:2204.06815* (2022).
- [38] G. Yiasemis, N. Moriakov, D. Karkalousos, M. Caan, J. Teuwen, Direct: Deep image reconstruction toolkit (2022). doi:10.21105/joss.04278. URL <https://doi.org/10.21105/joss.04278>
- [39] K. Fourmont, Non-equispaced fast fourier transforms with applications to tomography, *Journal of Fourier Analysis and Applications* 9 (5) (2003) 431–450. doi:10.1007/s00041-003-0021-1. URL <https://doi.org/10.1007/2Fs00041-003-0021-1>
- [40] J. Jackson, C. Meyer, D. Nishimura, A. Macovski, Selection of a convolution function for fourier inversion using gridding (computerised tomography application), *IEEE Transactions on Medical Imaging* 10 (3) (1991) 473–478. doi:10.1109/42.97598. URL <https://doi.org/10.1109/2F42.97598>

Appendix A. Supplementary Material

In this section, we provide additional figures and tables that support the findings and analysis presented in the main paper.

Appendix A.1. Acquisition Parameters and Experiment Splits

Table A.1: Acquisition parameters and experiment splits per dataset used in our experiments.

Dataset	FastMRI Knee	FastMRI Brain	Calgary Campinas
Field Strength	1.5T & 3.0T	1.5T & 3.0T	3.0T
Sequence	PD ¹ with and without fat suppression	T1-w ² , T1-w post contrast, T2-w, FLAIR	T1-w
Subjects	Healthy or Abnormality present	Healthy or Pathology present	Presumed healthy
Acquisition	Cartesian	Cartesian	Cartesian
Fully Sampled	Yes	Yes	Yes
Subsampling	Phase and slice	Phase and slice	Phase and slice
Directions	encoding directions	encoding directions	encoding directions
No. Coils	15	2 - 24	12
No. Volumes	1172	5846	67
No. Slices	41877	92574	10452
Split size Training	973 / 34742	4469 / 70748	40 / 6240
(No. volumes/ Validation	100 / 3587	686 / 10880	14 / 2184
No. slices) Test	99 / 3548	691 / 10946	13 / 2028

Proton Density
Weighted

Appendix A.2. Scheme-Specific Setup Experiments Results

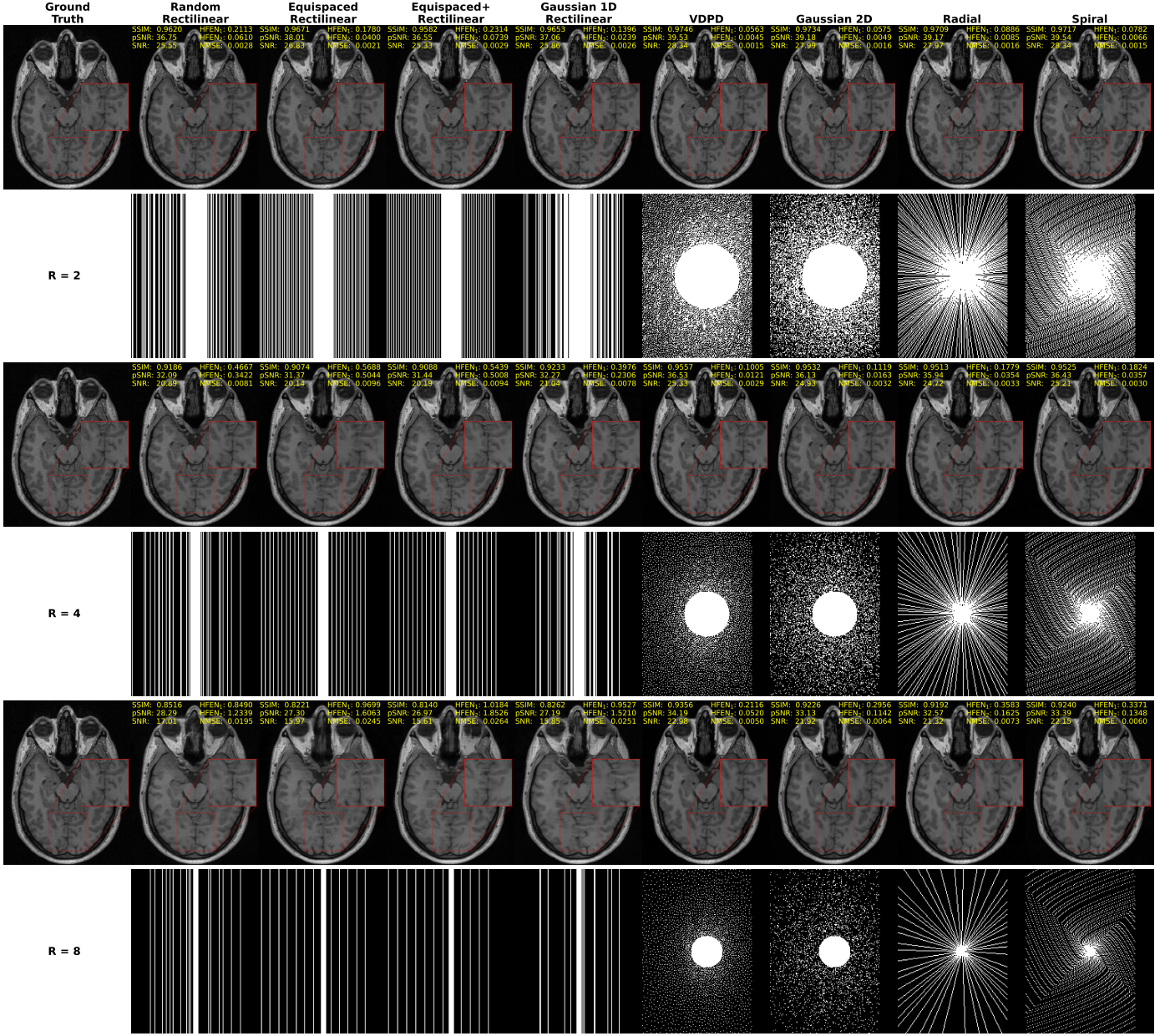


Figure A.1: Representative reconstruction of a sample from the Calgary Campinas test set obtained from the scheme-specific experiments. For the ground truth image the RSS method was applied on the fully sampled k -space. For each subsampling scheme, we retrospectively applied subsampling masks as shown in rows 2, 4, 6 (with accelerations factors of 2, 4, 8, respectively) onto the fully sampled k -space. Rows 1, 3, 5 illustrate the RSS reconstructed k -space output from each model. Quantitative metrics against the ground truth are inscribed on the top left of each reconstruction. Note that the right 15% portion of the k -space was not collected and therefore subsampling masks were zero-filled accordingly.

Table A.2: Scheme-specific experiments average results on the test sets. Bold numbers indicate the best across subsampling schemes.

Dataset	Subsampling Scheme	Acceleration Factor (R)																	
		2						4						8					
		SSIM	pSNR	SNR	HFEN ₁	HFEN ₂	NMSE	SSIM	pSNR	SNR	HFEN ₁	HFEN ₂	NMSE	SSIM	pSNR	SNR	HFEN ₁	HFEN ₂	NMSE
FastMRI	Random Rect.	0.948	41.8	25.7	0.186	0.049	0.003	0.910	38.0	22.1	0.384	0.240	0.007	0.864	34.1	18.4	0.633	0.756	0.015
	Equispaced Rect.	0.945	41.8	25.7	0.184	0.048	0.003	0.913	38.5	22.6	0.350	0.192	0.006	0.866	34.2	18.6	0.613	0.675	0.014
	Equispaced+ Rect.	0.951	42.5	26.4	0.167	0.039	0.003	0.914	38.5	22.6	0.352	0.196	0.006	0.871	34.7	19.1	0.580	0.600	0.013
	Gaussian 1D	0.954	42.5	26.4	0.121	0.020	0.003	0.920	39.1	23.1	0.288	0.122	0.005	0.885	35.9	20.2	0.498	0.411	0.010
	Knee VDPD	0.959	43.9	27.7	0.082	0.013	0.002	0.938	41.6	25.5	0.113	0.020	0.004	0.918	39.6	23.4	0.170	0.039	0.005
	Gaussian 2D	0.959	43.5	27.3	0.076	0.011	0.003	0.935	40.9	24.7	0.113	0.021	0.004	0.916	39.2	23.0	0.181	0.043	0.006
	Radial	0.956	43.3	27.1	0.096	0.015	0.003	0.935	41.1	24.9	0.149	0.030	0.004	0.916	39.3	23.1	0.211	0.058	0.005
	Spiral	0.957	43.5	27.3	0.096	0.015	0.003	0.937	41.3	25.0	0.151	0.031	0.004	0.919	39.5	23.3	0.205	0.055	0.005
FastMRI	Random Rect.	0.970	42.8	26.1	0.223	0.052	0.002	0.944	37.8	21.4	0.539	0.466	0.007	0.903	32.4	16.3	1.000	1.999	0.026
	Equispaced Rect.	0.969	43.0	26.2	0.202	0.040	0.002	0.949	38.9	22.4	0.441	0.280	0.006	0.911	33.3	17.2	0.887	1.443	0.020
	Equispaced+ Rect.	0.972	43.7	27.0	0.187	0.033	0.002	0.949	38.9	22.5	0.449	0.297	0.006	0.912	33.6	17.4	0.868	1.394	0.019
	Gaussian 1D	0.972	43.4	26.7	0.174	0.027	0.002	0.950	38.9	22.3	0.442	0.284	0.006	0.920	34.4	18.1	0.765	1.012	0.016
	Brain VDPD	0.977	45.2	28.3	0.098	0.008	0.001	0.966	42.8	25.9	0.134	0.014	0.002	0.954	40.5	23.7	0.199	0.030	0.004
	Gaussian 2D	0.976	44.5	27.6	0.090	0.007	0.002	0.965	42.0	25.2	0.131	0.013	0.003	0.953	40.0	23.2	0.237	0.046	0.004
	Radial	0.973	44.1	27.2	0.133	0.013	0.002	0.962	41.7	24.9	0.207	0.035	0.003	0.950	39.3	22.6	0.315	0.105	0.005
	Spiral	0.975	44.5	27.6	0.128	0.012	0.002	0.964	42.2	25.3	0.198	0.031	0.003	0.953	40.1	23.3	0.259	0.058	0.004
Calgary	Random Rect.	0.967	38.5	25.2	0.252	0.091	0.003	0.913	32.5	19.5	0.653	0.738	0.014	0.834	28.4	15.2	1.150	2.375	0.035
	Equispaced Rect.	0.968	39.1	25.8	0.229	0.070	0.003	0.925	33.4	20.5	0.573	0.553	0.011	0.853	29.2	16.2	1.015	1.829	0.028
	Equispaced+ Rect.	0.974	40.5	27.0	0.194	0.046	0.002	0.928	33.8	20.8	0.553	0.507	0.010	0.851	29.2	16.2	1.029	1.837	0.028
	Gaussian 1D	0.973	39.6	26.3	0.160	0.033	0.003	0.935	34.3	21.2	0.450	0.329	0.009	0.854	29.1	16.1	1.018	1.829	0.029
	Campinas VDPD	0.981	42.8	29.2	0.065	0.005	0.001	0.966	39.0	25.5	0.118	0.016	0.003	0.949	36.3	23.0	0.231	0.067	0.005
	Gaussian 2D	0.980	42.3	28.7	0.066	0.005	0.001	0.963	38.5	25.1	0.130	0.020	0.003	0.940	35.2	22.0	0.315	0.136	0.007
	Radial	0.976	41.4	27.8	0.102	0.011	0.002	0.960	37.8	24.4	0.200	0.048	0.004	0.933	34.2	21.1	0.390	0.225	0.009
	Spiral	0.976	41.5	27.9	0.096	0.010	0.002	0.960	38.0	24.6	0.198	0.045	0.004	0.933	34.5	21.4	0.389	0.209	0.008

Appendix A.3. Multi-Scheme Setup Experiments Results

Table A.3: Multi-scheme experiments average results on the test sets. Bold numbers indicate the best across subsampling schemes.

Dataset	Subsampling Scheme	Acceleration Factor (R)																	
		2						4						8					
		SSIM	pSNR	SNR	HFEN ₁	HFEN ₂	NMSE	SSIM	pSNR	SNR	HFEN ₁	HFEN ₂	NMSE	SSIM	pSNR	SNR	HFEN ₁	HFEN ₂	NMSE
FastMRI	Random Rect.	0.949	42.0	25.9	0.181	0.045	0.003	0.912	38.3	22.3	0.368	0.213	0.006	0.870	34.6	18.8	0.596	0.650	0.013
	Equispaced Rect.	0.946	42.0	25.9	0.178	0.045	0.003	0.915	38.8	22.8	0.334	0.169	0.006	0.872	34.8	19.0	0.576	0.571	0.013
	Equispaced+ Rect.	0.952	42.7	26.6	0.162	0.037	0.003	0.917	38.8	22.9	0.335	0.173	0.006	0.878	35.2	19.5	0.543	0.503	0.012
	Gaussian 1D	0.955	42.7	26.5	0.118	0.020	0.003	0.921	39.3	23.2	0.278	0.112	0.005	0.889	36.4	20.5	0.466	0.345	0.009
	Knee VDPD	0.959	43.6	27.4	0.086	0.014	0.003	0.938	41.4	25.2	0.116	0.022	0.004	0.918	39.5	23.3	0.169	0.039	0.005
	Gaussian 2D	0.959	43.4	27.1	0.079	0.012	0.003	0.934	40.6	24.3	0.116	0.022	0.005	0.916	39.0	22.7	0.181	0.044	0.006
	Radial	0.955	43.3	27.0	0.101	0.016	0.003	0.935	41.1	24.9	0.153	0.032	0.004	0.917	39.3	23.1	0.213	0.059	0.006
	Spiral	0.957	43.4	27.2	0.100	0.016	0.003	0.937	41.3	25.0	0.150	0.030	0.004	0.920	39.6	23.4	0.201	0.053	0.005
FastMRI	Random Rect.	0.971	43.1	26.3	0.213	0.047	0.002	0.947	38.3	21.8	0.504	0.395	0.007	0.912	33.3	17.2	0.899	1.562	0.021
	Equispaced Rect.	0.969	43.0	26.3	0.209	0.043	0.002	0.949	38.8	22.3	0.457	0.303	0.006	0.913	33.4	17.3	0.876	1.403	0.019
	Equispaced+ Rect.	0.973	43.9	27.1	0.185	0.031	0.002	0.950	39.1	22.6	0.445	0.291	0.006	0.915	33.9	17.7	0.840	1.290	0.018
	Gaussian 1D	0.972	43.4	26.6	0.178	0.028	0.002	0.949	38.8	22.3	0.450	0.290	0.006	0.922	34.6	18.3	0.748	0.939	0.015
	Brain VDPD	0.977	45.1	28.2	0.101	0.009	0.001	0.966	42.6	25.8	0.140	0.015	0.003	0.953	40.4	23.6	0.208	0.034	0.004
	Gaussian 2D	0.976	44.2	27.4	0.093	0.007	0.002	0.964	41.8	25.0	0.134	0.014	0.003	0.952	40.0	23.2	0.229	0.043	0.004
	Radial	0.973	44.1	27.3	0.142	0.015	0.002	0.962	41.8	25.0	0.208	0.036	0.003	0.952	39.4	22.8	0.323	0.118	0.005
	Spiral	0.974	44.4	27.6	0.141	0.016	0.002	0.964	42.3	25.5	0.195	0.030	0.003	0.954	40.3	23.5	0.276	0.073	0.004
Calgary	Random Rect.	0.970	39.3	26.0	0.223	0.071	0.003	0.925	33.4	20.4	0.569	0.567	0.011	0.856	29.4	16.2	0.998	1.836	0.029
	Equispaced Rect.	0.971	39.7	26.3	0.211	0.057	0.003	0.932	34.1	21.1	0.519	0.452	0.009	0.868	30.0	16.9	0.915	1.489	0.024
	Equispaced+ Rect.	0.976	41.0	27.6	0.177	0.037	0.002	0.937	34.6	21.6	0.492	0.400	0.008	0.870	30.1	17.1	0.904	1.433	0.023
	Gaussian 1D	0.975	40.1	26.7	0.147	0.027	0.002	0.941	34.8	21.8	0.408	0.270	0.008	0.875	30.0	17.0	0.881	1.373	0.023
	Campinas VDPD	0.981	42.7	29.1	0.066	0.005	0.001	0.965	38.8	25.3	0.121	0.017	0.003	0.947	36.0	22.7	0.244	0.075	0.006
	Gaussian 2D	0.980	42.2	28.6	0.067	0.005	0.001	0.963	38.4	25.0	0.131	0.021	0.003	0.938	35.0	21.8	0.332	0.152	0.007
	Radial	0.977	41.5	27.9	0.097	0.010	0.002	0.960	37.8	24.4	0.204	0.051	0.004	0.932	34.1	21.0	0.407	0.242	0.009
	Spiral	0.977	41.7	28.1	0.094	0.009	0.002	0.961	38.3	24.9	0.194	0.043	0.003	0.936	34.8	21.7	0.378	0.194	0.008

Appendix A.4. Comparison of Scheme-Specific Setup vs Multi-Scheme Setup

In Figure A.2, we present a comparison between the Scheme-Specific Setup and Multi-Scheme Setup in terms of quantitative results. Violin plots are employed to visualize the variations in evaluation metrics between the two setups for each dataset. The Scheme-Specific Setup involves training a model on data subsampled using a single subsampling scheme, while the Multi-Scheme Setup trains a model on data subsampled using all available subsampling schemes.

To establish the necessary context, we define the relevant variables as follows: \mathbf{y} represents the fully-sampled k -space data, and $\tilde{\mathbf{y}}^S$ denotes the k -space data subsampled using scheme S . Furthermore, \mathbf{x}_{GT} corresponds to the ground truth image (reconstructed from \mathbf{y} using RSS), $\mathbf{x}_{\text{multi}}^S$ represents the image prediction obtained from the model trained on all subsampling schemes, and $\mathbf{x}_{\text{single}}^S$ signifies the image prediction derived from the model trained specifically on scheme S , with $\tilde{\mathbf{y}}^S$ as input in both cases.

By computing the difference $m(\mathbf{x}_{\text{GT}}, \mathbf{x}_{\text{multi}}^S) - m(\mathbf{x}_{\text{GT}}, \mathbf{x}_{\text{single}}^S)$ for each evaluation metric m , we can compare the performance of the two setups/models. Positive differences indicate superior performance for the multi-scheme model, particularly in the case of SSIM, pSNR, and SNR. Conversely, negative differences indicate better performance for the scheme-specific model, specifically for HFEN₁, HFEN₂, and NMSE. To assess the statistical significance, we conducted pair-wise ASO significance tests between the multi-scheme and scheme-specific quantitative results for each combination of dataset, acceleration, and metric.

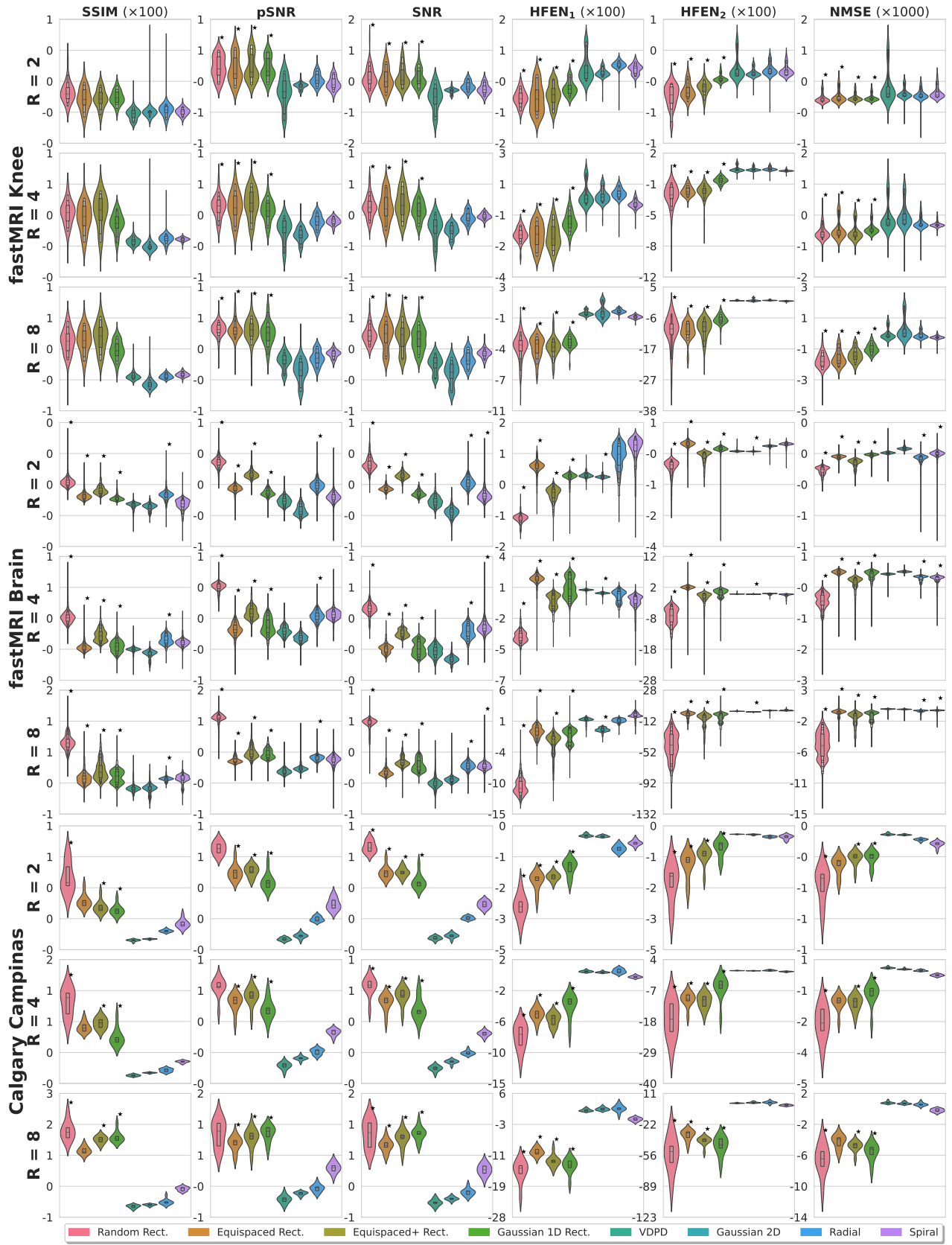


Figure A.2: Comparison of Scheme-Specific Setup vs Multi-Scheme Setup: Quantitative Results. The symbol \star indicates a significant performance difference ($\epsilon_{\min} < 0.5$).

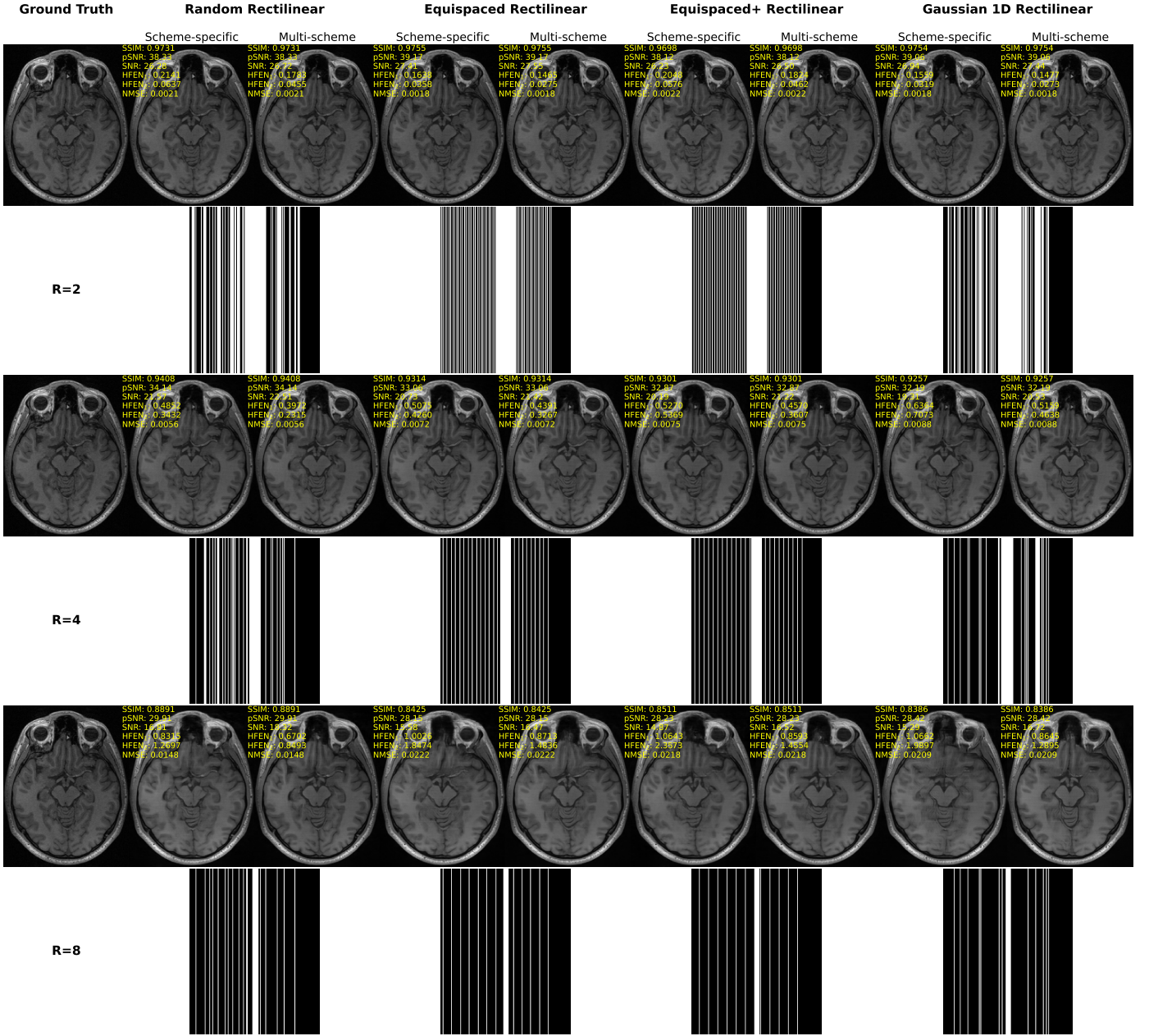


Figure A.3: Scheme-specific vs multi-scheme setups visual comparison. Representative reconstructions of a sample from the Calgary-Campinas dataset subsampled with the four rectilinear schemes obtained from the scheme-specific and multi-scheme experiments for three acceleration factors.

Appendix A.5. Robustness to Model Choice

In this appendix subsection, we present in Figure A.4 violin plots depicting the result metrics of our experiments, accompanied by Table A.4 showing the average metrics. These experiments were conducted using RIMs as the deep learning architecture on the Calgary-Campinas dataset. Each subsampling scheme was trained with a separate RIM model, resulting in a total of 8 models. All models were trained until convergence with the same set of hyperparameters.

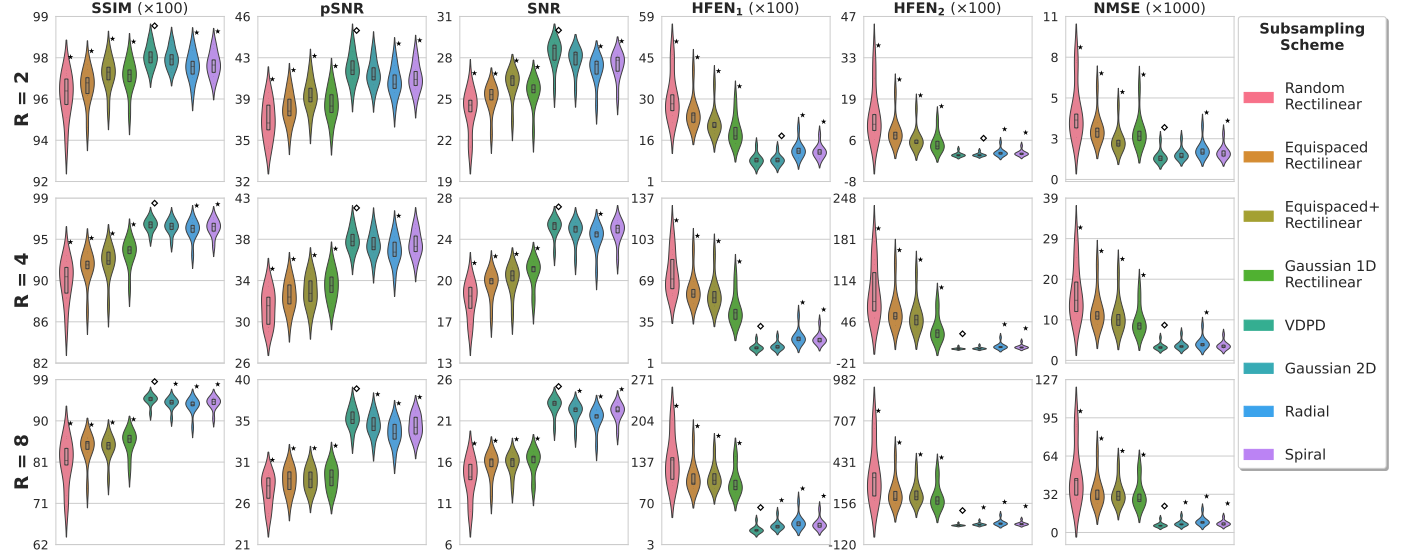


Figure A.4: Model dependence experiments quantitative results on the Calgary-Campinas dataset using RIMs instead of RecurrentVarNets. For each subsampling scheme a distinct RIM was trained (in total 8 models). All models were built with identical hyperparameters and were trained to convergence. In each case we picked to evaluate the best model based on the validation performance on the SSIM metric. For each acceleration-metric combination, pair-wise ASO significance tests were performed between the average best (VDPD, denoted by \diamond) performing and the rest schemes. The symbol \star indicates that VDPD was found to be significantly better ($\epsilon_{\min} < 0.5$).

Table A.4: Model dependence experiments average quantitative results on the Calgary-Campinas dataset using RIMs instead of RecurrentVarNets. Bold numbers indicate the best across subsampling schemes.

Subsampling Scheme	Acceleration Factor (R)																	
	2						4						8					
	SSIM	pSNR	SNR	HFEN ₁	HFEN ₂	NMSE	SSIM	pSNR	SNR	HFEN ₁	HFEN ₂	NMSE	SSIM	pSNR	SNR	HFEN ₁	HFEN ₂	NMSE
Random Rect.	0.959	37.2	24.0	0.309	0.143	0.005	0.903	31.7	18.6	0.748	0.945	0.016	0.805	27.2	13.8	1.403	3.493	0.047
Equispaced Rect.	0.963	38.3	24.9	0.255	0.088	0.003	0.917	32.8	19.9	0.618	0.646	0.012	0.836	28.3	15.3	1.138	2.297	0.034
Equispaced+ Rect.	0.969	39.4	26.0	0.221	0.063	0.003	0.922	33.3	20.3	0.583	0.566	0.011	0.838	28.5	15.4	1.127	2.231	0.033
Gaussian 1D	0.968	38.6	25.3	0.191	0.051	0.003	0.932	33.9	20.9	0.457	0.351	0.010	0.849	28.6	15.6	1.063	2.031	0.032
VDPD	0.977	41.8	28.2	0.091	0.011	0.002	0.962	38.4	24.9	0.137	0.023	0.003	0.943	35.7	22.3	0.276	0.096	0.006
Gaussian 2D	0.976	41.3	27.8	0.090	0.010	0.002	0.960	38.0	24.6	0.147	0.028	0.004	0.936	34.9	21.6	0.342	0.159	0.008
Radial	0.972	40.6	27.0	0.126	0.018	0.002	0.957	37.4	24.0	0.223	0.064	0.004	0.930	33.9	20.8	0.402	0.255	0.010
Spiral	0.973	41.0	27.4	0.120	0.016	0.002	0.959	38.0	24.6	0.210	0.052	0.004	0.936	34.8	21.6	0.367	0.195	0.008